ELSEVIER

Contents lists available at ScienceDirect

Journal of Quantitative Spectroscopy & Radiative Transfer

journal homepage: www.elsevier.com/locate/jqsrt



Temperature-dependent line mixing in the R-branch of the v_3 band of methane



Jidong Li^{a,b}, Anil P. Nair^a, Kevin K. Schwarm^a, Daniel I. Pineda^{a,*}, R. Mitchell Spearrin^a

- ^a Department of Mechanical and Aerospace Engineering, University of California, Los Angeles (UCLA), Los Angeles, CA 90095, USA
- ^b Department of Energy and Power Engineering, Tsinghua University, Beijing, 100084, China

ARTICLE INFO

Article history: Received 13 July 2020 Revised 18 August 2020 Accepted 18 August 2020 Available online 19 August 2020

Keywords: Line mixing Absorption spectroscopy Methane CH₄ High temperature High pressure

ABSTRACT

High-temperature line mixing behavior was studied for 15 R-branch line manifolds in the v_3 band of methane from 3.14 µm to 3.28 µm. The temperature-dependence of the line mixing parameters for the R(4) to R(18) manifolds perturbed by nitrogen were empirically-determined over a range of temperatures from 300–1000 K using Fourier transform infrared spectroscopy in a heated gas cell. A more extensive line mixing investigation of the rovibrational transitions comprising the R(15) manifold was performed at lower pressures (0.3–2 atm) using laser absorption spectroscopy from 300–1600 K in both the heated cell and a high-enthalpy shock tube. Measured spectra were modeled and fit using both a modified exponential gap model and a perturbation theory-based first-order model to capture the pressure- and temperature-dependence of the line mixing effects. The modified exponential gap model was found to sufficiently capture the line mixing behavior at pressures greater than 20 atm, while perturbation theory enables more accurate characterization of the behavior at the lower pressures. The applicability of both the modified exponential gap model and perturbation theory is also discussed with analyses of the fitting residuals and the parameter uncertainties to provide reference for the use of the two empirical models in simulating the R-branch of the v_3 band of 12 CH₄ over a wide range of thermodynamic conditions.

© 2020 Elsevier Ltd. All rights reserved.

1. Introduction

Methane (CH₄) is an important molecule in biology, planetary astronomy, climatology, agriculture, and combustion chemistry. As a principal fuel component of natural gas, intermediate in the oxidation of larger hydrocarbons, and-increasingly-a promising future rocket fuel [1,2], CH₄ plays a key role in energy conversion systems globally, and high-temperature spectroscopy of CH₄ is particularly relevant to combustion research [3]. Additionally, temperature-dependent spectroscopy of CH₄ is relevant for both remote and in-situ sensing of terrestrial [4-6], extraterrestrial [7,8], and extrasolar [9,10] planetary atmospheres. CH₄ is one of the most substantial contributors to Earth's greenhouse effect, after CO₂ and H₂O [11], and its accurate detection and spectroscopic modeling is key to understanding its environmental impact on Earth [12]. This work documents an experimental investigation of ¹²CH₄ spectra from 3.14 μm to 3.28 μm at elevated pressures relevant to energy conversion systems over a wide range of ele-

E-mail addresses: lijidong@g.ucla.edu (J. Li), anilnair1995@ucla.edu (A.P. Nair), kschwarm@ucla.edu (K.K. Schwarm), daniel.pineda@utsa.edu, dipineda@ucla.edu (D.I. Pineda), spearrin@ucla.edu (R. Mitchell Spearrin).

vated temperatures (up to 1600 K), with the goal of developing a predictive model of the target spectral domain that accurately captures the pressure- and temperature-dependence of collisional line mixing effects.

Several researchers have utilized absorption by methane for quantitative in-situ measurement of species concentration and/or temperature at elevated temperatures [3,13–21]. Many of these studies [3,16–19] employ empirical peak-to-valley absorption methods or cross-section correlations for quantitative interpretation of specific wavelengths, an approach that avoids the complexity of the underlying line-by-line spectroscopy of CH₄ but lacks in scalability over varying thermodynamic conditions or bath gases. Line-by-line modeling offers greater utility, but the spectroscopic complexities must be addressed.

Though the simplest stable hydrocarbon, CH₄ poses numerous spectroscopic modeling challenges, particularly at elevated temperatures and pressures. The tetrahedral molecule exhibits a complicated series of interacting vibrational states (polyads) as a consequence of the approximately similar energies of two fundamental bands and two overtone bands ($v_1 \approx v_3 \approx 2v_2 \approx 2v_4$) [22]. As a result, the spectra of a given polyad of CH₄ often comprise overlapping fundamental bands, hot bands, overtone bands, and combination bands, complicating measurements of spectroscopic param-

^{*} Corresponding author.

eters such as linestrength, collisional broadening and shift coefficients due to local spectral blending. Moreover, the abundance of spectral transitions in these bands poses computational challenges for comprehensive and accurate predictive modeling of CH₄ spectra at elevated temperatures; only recently has a high-temperature line list for CH₄ that balances both accuracy and computational efficiency been compiled and made available via HITEMP [23]. Notably, however, even with a comprehensive line list significant disagreement in spectral absorbance, relative to that predicted by conventional lineshape summation of individual transitions, can be observed for measured CH₄ spectra at moderately elevated gas densities. This is largely attributed to line mixing, a band or manifold narrowing effect in spectrally dense regions that occurs at high gas densities resulting from collision-induced changes in the populations of energy states [24]. We focus this experimental study on the characterization of line mixing behavior from 300-1600 K in the R-branch of the v_3 band of CH_4 over a wide range of pressures and gas densities with the simple goal of developing an accurate empirical model.

Line mixing in the v_3 band of CH_4 at temperatures at or below 300 K at a variety of pressures has been investigated previously [25-40], owing to its relevance in sensing of the atmospheres of Earth [34], the Jovian planets [35], and Titan, a natural satellite of Saturn. Line mixing is notably pronounced in the Q branch, as well as in the higher rotational energy manifolds (Imanifolds) of the P and R branches due to the multiplicity of rovibrational transitions in close proximity. Various line mixing models have been developed and employed to describe CH₄ spectra for ranges of temperatures and pressures relevant to in-situ and remote atmospheric sensing. First-order line mixing models based on the perturbative treatment proposed by Rosenkranz [41] have been shown to adequately characterize line mixing at low pressures [25-27,30,31,33,37-40,42]. At higher pressures, energy-gap scaling models which correlate the population transfer rates that comprise the relaxation matrix have been used [28-30,32-35]. Though successfully implemented for some linear molecules [43-45], energygap laws [46,47] have been found less appropriate for modeling non-linear molecules such as CH₄ at low to moderate densities

To the authors' knowledge, the temperature dependence of line mixing effects on CH₄ v_3 spectra has not been previously investigated above 300 K. Some temperature-dependence studies of line mixing for CH₄ have been performed in the v_3 region between 200 K and 300 K [29]. Line mixing parameters and temperature dependence in the P(9) manifold of the v_3 band were measured between 90 and 296 K by Mondelain et al [36]. The line mixing parameters in the R(6) manifold of the v_3 band were also recorded over the temperature range from 213.5 K to room temperature [37]. In general, the collective of previous CH₄ line mixing studies have been focused on examining behavior near ambient temperature (\sim 300 K) or below.

This paper describes experimental measurements and modeling of the aforementioned line mixing effects in the triply degenerate antisymmetric C-H stretch ν_3 band of CH₄ at temperatures up to 1600 K, relevant to combustion environments. *R*-branch spectra from R(0) to R(18) are initially examined at various pressures (2–25 atm) and temperatures (298–1021 K) using Fourier transform infrared spectroscopy (FTIR) combined with a heated gas cell. Line mixing and its temperature dependence in the R(15) manifold are further examined using interband cascade laser absorption spectroscopy near 3.15 μ m at low pressures (0.3–2 atm) and elevated temperatures (298–1610 K) in both a gas cell and a shock tube. A modified exponential gap law and first-order line mixing approximation (perturbation theory) were both used to model the line mixing effects of CH₄ perturbed by N₂ and compared at different experimental conditions. The adequacy of the two empirical

models for capturing the CH_4 line mixing effects under varying assumptions is also discussed, including non-ideal behavior observed over varying pressure and temperature.

2. Theory

2.1. Line mixing

Spectral absorbance, α_{ν} , accounting for line mixing collisions can be written within the impact approximation in the following form:

$$\alpha_{\nu} = -\ln\left(\frac{I_t}{I_0}\right)_{\nu} = \frac{NL}{\pi} \operatorname{Im}(\mathbf{d} \cdot \mathbf{G}^{-1} \cdot \boldsymbol{\rho} \cdot \mathbf{d})$$
 (1)

where N [molec \cdot cm⁻³] is the total number density of the absorbing species and L [cm] is the path length, ρ is a diagonal matrix with nonzero elements ρ_i defined by the lower state Boltzmann population fraction:

$$\rho_i = \frac{N_i}{N} = \frac{g_i''}{Q} \exp\left[\frac{-hcE''}{k_BT}\right]$$
 (2)

Here, N_i [molec \cdot cm⁻³] is the number density at a certain energy level, g_i'' is the lower state degeneracy, E'' [cm⁻¹] is the lower state energy, Q is the total internal partition function, h [J \cdot s] is Planck's constant, and c [cm/s] is the speed of light, and \mathbf{d} [cm⁻¹/(molec \cdot cm⁻²)]^{1/2} is a vector of transition amplitudes with elements d_i given as:

$$d_i = \sqrt{\frac{S_i(T)}{\rho_I}} \tag{3}$$

The dependence on wavenumber, ν [cm⁻¹], is within **G** [cm⁻¹], a complex matrix defined as:

$$\mathbf{G} = \nu \mathbf{I} - \mathbf{H} \tag{4}$$

Where **I** is the identity matrix and a frequency-independent matrix \mathbf{H} [cm⁻¹] is defined as:

$$\mathbf{H} = \mathbf{v}_0 - i\mathbf{W} \tag{5}$$

 ν_0 [cm⁻¹] is a diagonal matrix of transition frequencies and **W** [cm⁻¹] is the relaxation matrix which captures collisional effects on the spectra and is given by:

$$\mathbf{W}_{ij} = \begin{cases} \Delta \nu_{c,i} - i\Delta_i & \text{if } i = j \\ PA_{RR}R_{i \to j} & \text{if } i \neq j \end{cases}$$
 (6)

Where P is the total pressure in units of [atm], the real diagonal elements of \mathbf{W} are the collisional half-widths $\Delta \nu_{c,i}$ [cm $^{-1}$], and the imaginary diagonal elements are the pressure shifts Δ_i [cm $^{-1}$]. The real off-diagonal elements are linearly proportional to the state-specific population transfer rates, $R_{i \to j}$ [cm $^{-1}$ /atm], between two states i and j. The off-diagonal components of \mathbf{W} represent contributions from rotational dephasing, which are neglected here and set to zero. In Eq. (5), \mathbf{H} can be diagonalized using a similarity transform to obtain a diagonal eigenvalue matrix Ω [cm $^{-1}$] with diagonal elements ω_i [cm $^{-1}$] such that:

$$\mathbf{\Omega} = \mathbf{A}^{-1} \cdot \mathbf{H} \cdot \mathbf{A} \tag{7}$$

Since **G** only differs from **H** by a constant diagonal matrix, \mathbf{G}^{-1} is also diagonalized by **A**. Eq. (1) can now be written as a function of ν spanning all relevant spectral transitions i:

$$\alpha_{\nu} = \frac{NL}{\pi} \operatorname{Im} \left[\sum_{i} \frac{(\mathbf{d} \cdot \mathbf{A})_{i} (\mathbf{A}^{-1} \cdot \boldsymbol{\rho} \cdot \mathbf{d})_{i}}{(\nu - \omega_{i})} \right]$$
(8)

If we define, $\Lambda_i = (\mathbf{d} \cdot \mathbf{A})_i (\mathbf{A}^{-1} \cdot \boldsymbol{\rho} \cdot \mathbf{d})_i$, α_{ν} becomes a sum over Lorentzian and dispersion terms:

$$\alpha_{\nu} = \frac{NL}{\pi} \sum_{i} \frac{\operatorname{Im} \mathbf{\Omega}_{i} \cdot \operatorname{Re} \mathbf{\Lambda}_{i} + \operatorname{Im} \mathbf{\Lambda}_{i} (\nu - \operatorname{Re} \mathbf{\Omega}_{i})}{(\nu - \operatorname{Re} \mathbf{\Omega}_{i})^{2} + \operatorname{Im} \mathbf{\Omega}_{i}^{2}}$$
(9)

(13)

2.2. Perturbative treatment theory

The perturbative treatment (PT) theory for modeling line mixing consists of making a perturbative expansion of the eigenvalues and eigenvectors of the matrix **H** in powers of $W_{ij}/(\nu_i - \nu_j)$. They can be introduced in Eq. (9), which gives the first order treatment:

$$\alpha_{\nu} = \frac{NL}{\pi} \sum_{i} \frac{S_{i} [\Delta \nu_{c} + Y_{i} (\nu - \nu_{0})]}{(\nu - \nu_{0,i} - \Delta_{i})^{2} + \Delta \nu_{c}^{2}}$$
(10)

with

$$Y_{i} = 2\sum_{j \neq i} \frac{d_{j}}{d_{i}} \frac{W_{ij}}{v_{i} - v_{j}}$$
(11)

where S_i , $\Delta \nu_c$, Δ_i and Y_i are the linestrength, collisional width, pressure shift and line mixing coefficient for the spectral line i. The expression in Eq. (10) will have different forms depending on the lineshape model assumed. When accounting first-order line mixing, the spectral absorbance assuming the Voigt profile (a convolution of the Doppler and Lorentzian profiles) becomes:

$$\alpha_{\nu} = \frac{NL}{\pi} \sum_{i} \left(\frac{S_{i}}{\Delta \nu_{D,i}} \right) \left(\frac{\ln(2)}{\pi} \right)^{1/2}$$

$$\left(\text{Re}[c(\nu, x_{i}, y_{i})] + Y_{i} \cdot \text{Im}[c(\nu, x_{i}, y_{i})] \right)$$
(12)

where $\Delta v_{D,i}$ is the Doppler half-width (HWHM), c is the complex error function, and

$$x_{i} = \frac{\nu - \nu_{0,i} - \Delta_{i}}{\Delta \nu_{D,i}} (\ln(2))^{1/2}$$

$$y_{i} = \frac{\Delta \nu_{c,i}}{\Delta \nu_{D,i}} (\ln(2))^{1/2}$$

At low pressures, it may be necessary to consider the influence of narrowing mechanisms, such as Dicke narrowing and speed-dependent effects [48,49]. When considering first-order line mixing for the Rautian profile, the corresponding absorbance is given

$$\alpha_{\nu} = \frac{NL}{\pi} \sum_{i} \left(\frac{S_{i}}{\Delta \nu_{D,i}} \right) \left(\frac{\ln(2)}{\pi} \right)^{1/2}$$

$$\times \left(\text{Re} \left[\frac{c(\nu, x_{i}, y_{i})}{1 - \sqrt{\pi} \beta c(\nu, x_{i}, y_{i})} \right] + Y_{i} \cdot \text{Im} \left[\frac{c(\nu, x_{i}, y_{i})}{1 - \sqrt{\pi} \beta c(\nu, x_{i}, y_{i})} \right] \right)$$

$$(14)$$

When considering speed dependent effects, the collisional width becomes a function of molecular speed and is modeled with the following expression:

$$\Delta \nu_{c,i}(\upsilon) = \Delta \nu_{c,i}(\upsilon_m) \left(1 + a_{s,i} \left[\left(\frac{\upsilon^2}{\upsilon_p} \right) - \frac{3}{2} \right] \right)$$
 (15)

Where υ is the speed of the absorbing molecule, υ_m is the mean speed of the absorber, υ_p is the most probable speed of the absorbing molecule, and $a_{s,i}$ is the speed-dependent coefficient for line i. The absorption coefficient for the speed-dependent Voigt profile with line mixing becomes:

$$\alpha_{\nu} = \frac{NL}{\pi^{3/2}} \sum_{i} S_{i} \int_{-\infty}^{+\infty} e^{-\nu^{2}} \upsilon$$

$$\times \left(\tan^{-1} \left[\frac{\upsilon + x_{i}}{y_{i} (a_{s,i} (\upsilon^{2} - 1.5) + 1)} \right]^{2} + \frac{Y_{i}}{2} \ln \left[\frac{\upsilon + x_{i}}{y_{i} (a_{s,i} (\upsilon^{2} - 1.5) + 1)} \right]^{2} \right) d\upsilon$$
(16)

It should be noted that the line mixing among transitions with different A, E, F symmetry are negligible for CH_4 because of the symmetry of the intermolecular potential [26,40] and the line mixing parameter sum rule constraint $\Sigma_i S_i Y_i = 0$ [27] was used for each A, E or F symmetry block. The temperature dependence of the parameter Y_i is given by the following empirical relation:

$$Y(T) = Y(T_0) \left(\frac{T_0}{T}\right)^n \tag{17}$$

Lastly, we note that in cases where the local linewidths substantially exceed the line spacing, a first-order treatment may not be adequate to fully capture line mixing effects [41,50]. However, in this data-driven work, we constrain the perturbative treatment to a first-order empirical model framework for simplicity.

2.3. Modified exponential gap law

In the modified exponential gap (MEG) law, the real part of the off-diagonals of the relaxation matrix W_{ij} in Eq. (6) can be constructed using the following form:

$$W_{ij} = PA_{RR}R_{i \to j} = P \times a_1(T) \left[\frac{1 + a_4 \left(\frac{E_i''}{a_2 k_B T} \right)}{1 + a_4 \left(\frac{E_i''}{k_B T} \right)} \right]^2$$

$$\times \exp \left[\frac{-a_3 \left(E_j'' - E_i'' \right)}{k_B T} \right]$$
(18)

where $a_1(T)$ [cm⁻¹/atm], a_2 , and a_3 are species-specific MEG law coefficients retrieved from spectral fits of the measured absorbance. a_4 describes the collision duration based on distance of closest approach and is kept constant for all the R manifolds in the spectral fitting performed in this study. A_{RR} is a scaling constant associated with mixing in the R-branch. Since collisions promote the Boltzmann population distribution, the upward and downward population transfer rates, $R_{i \rightarrow j}$ and $R_{j \rightarrow i}$, can be related through the detailed-balance principle [51]:

$$\rho_i R_{i \to i} = \rho_i R_{i \to i} \tag{19}$$

A single set of measured absorbance is sufficient to obtain the species-specific MEG law coefficients for a given temperature [52], and $a_1(T)$ can be modeled as a power law expression to determine the temperature dependence of the relaxation matrix components:

$$a_1(T) = a_1(T_0) \left(\frac{T_0}{T}\right)^m$$
 (20)

where $a_1(T_0)$ is the MEG law coefficient at a reference temperature, T_0 , and m is defined as the temperature exponent, obtained by fitting multiple sets of absorbance data over a range of temperatures.

In the present work, the broadening half width (HWHM) and the pressure shift for CH₄-N₂ are calculated using CH₄-air broadening and shift coefficients from the HITEMP database [23]. Only the line mixing coefficients are set as free parameters for both the MEG law and perturbative treatment models in fitting the measured spectra.

3. Experimental setup

An FTIR and tunable interband cascade laser near 3.16 $\,\mu m$ were used to measure the CH₄ absorption spectra in a heated gas cell over a range of temperatures from 300–1000 K. A high-enthalpy shock tube was additionally used for measurements at higher temperatures from 1000–1700 K with the laser source. Here we detail the experimental configurations.

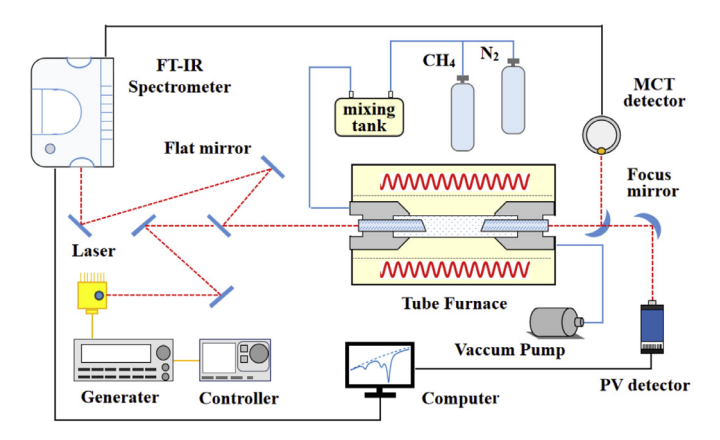


Fig. 1. Experimental setup for the laser and FTIR in the gas cell.

3.1. FTIR Gas cell measurements

To determine the line mixing parameters of the CH_4 v_3 R branch, absorbance measurements were made using a hightemperature high-pressure optical gas cell at temperatures varying from 300-1000 K and pressures varying from 0.3-25 atm. The cell body is housed in a tube furnace and connected to a local gas delivery manifold leading to vacuum pumps, source gas bottles, and an agitated mixing tank used to barometrically prepare CH₄/N₂ mixtures for experimental measurements, as shown in Fig. 1. The gas pressure within the cell is monitored with a variable capacitance pressure transducer for high-pressure measurements and a dual-capacitance manometer for measurements below 1000 torr with accuracies of 0.25% and 0.12%, respectively. The cell temperature is monitored with multiple K-type thermocouples along the test region with an accuracy of 0.75%. More details about the mechanical design of the cell, including a thermal analysis of temperature uniformity, are described in previous work [53].

Over the full range of pressures, two different optical systems were used to measure the CH₄ absorbance spectra. At test pressures from 0.3-2.0 atm, a narrow linewidth laser was used to spectrally-resolve the R(15) manifold, discussed further in Section 3.2. For pressures ranging from 2.0-25 atm, a Fouriertransform infrared spectrometer (Nicolet iS50 FTIR) was used to capture the entirety of the v_3 band. We focus our study and data analysis to the R branch in part due to poor transmission (and lower data quality) at the longer P-branch wavelengths which is attributed to the temperature-dependent transmission of the sapphire windows on the heated gas cell. The FTIR measurements shown here represent a spectral resolution of 0.125 cm⁻¹ using the Happ-Genzel apodization function with Mertz phase correction and no applied zero-filling. Measured spectra were compared to experimental data by Pieroni et al [28]. to check that FTIR settings were appropriate for the conditions of interest, yielding accurate results with weak dependence on apodization function. For each temperature and pressure condition, the gas cell was initially vacuumed for the background measurements before introducing the test mixtures. Test measurements were taken with N_2 as the test gas to ensure no pressure dependence of the FTIR background signal and validate the use of vacuum for background measurements. The cell pressure and temperature was monitored to ensure thermal equilibrium of the test gas within the gas cell prior to data collection. The measured data represent 16 averaged scans with a total data collection time of 5 minutes with pressure constant and slight fluctuations in temperature recorded for use in the uncertainty analysis.

Fig. 2 shows an FTIR measurement of the CH_4 v_3 band at the pressure of 2 atm and temperature of 298 K with 0.52% CH_4 di-

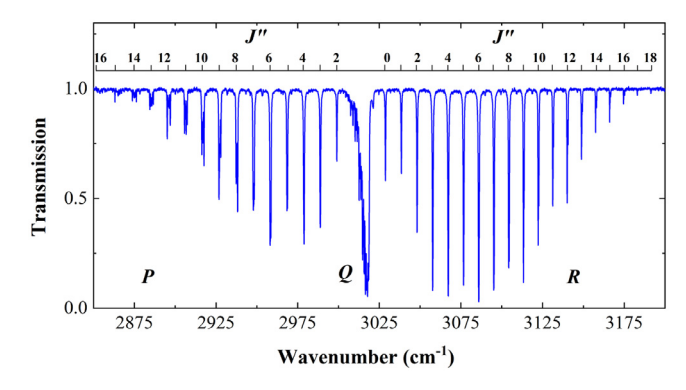


Fig. 2. The measured transmission of the CH₄ ν_3 band: P=2 atm, T=298 K, $X_{\text{CH}_4}=0.0052$. The strong lines (J''=0–18) belong to the ν_3 band consisting of P, Q and R branches. Weak lines belong to the $2\nu_3$, $2\nu_4$ and $\nu_2+\nu_4$ bands.

luted in N_2 , which encompasses P, Q and R branches up to J''=18. Notably, each J'' consists of a manifold of transitions with varying symmetry and n quantum index [54], which increases with J''. The line mixing of the R branch from R(0) to R(18) manifold was measured using the FTIR at various pressures from 2 atm to 25 atm and the R(15) manifold was more extensively measured at lower pressures from 0.3 atm to 2.0 atm using the laser source.

3.2. Laser absorption spectroscopy optical setup

For high spectral-resolution investigations of CH₄ near 3.16 μ m in both the high-temperature optical cell and the high-enthalpy shock tube, a continuous-wave distributed feedback (DFB) interband cascade laser (ICL) (Nanosystems and Technologies GmbH) is used to access the individual rovibrational transitions comprising the R(15) manifold. This specific wavelength is targeted for high-temperature combustion sensing applications. The ICL is tunable from 3162 to 3171 cm⁻¹, and has a nominal output power of 15 mW at 3166 cm⁻¹. A 10 kHz sawtooth waveform of injection current is used to tune the ICL across a 2 cm⁻¹ wavenumber range to resolve the entire R(15) manifold. Additionally, the injection current is scanned below the lasing threshold to account for thermal emission from the gases in both experimental devices.

The optical arrangement of the high-resolution sensor on both the high-temperature optical cell and the high-enhtalpy shock tube is shown in Figs. 1 and 3, respectively. The transmitted laser radiation is passed though an optical iris and a bandpass spectral filter (Spectrogon, 3160 ± 60 nm) to minimize thermal emission before being focused onto a thermo-electrically cooled photovoltaic (PV)

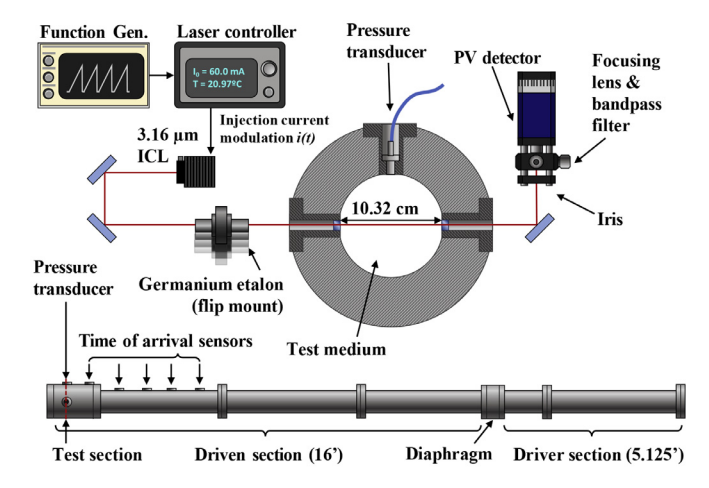


Fig. 3. Experimental setup for the laser alignment on the shock tube.

detector (VIGO System PVI-4TE-5). For each measurement I_t , a corresponding background I_0 is recorded in the absence of a mixture to establish a baseline for calculation in Eq. (1). The relative frequency of the laser light is determined by placing a germanium etalon with a free spectral range of 0.0241 cm⁻¹ in the path of the beam using an optical flip-mount.

3.3. Shock tube measurements

A high-enthalpy shock tube is used to generate higher temperatures (> 1050 K) via near-instantaneous shock heating of test gases. The shock tube is described in previous work by the authors [44,45,55], and shown in Fig. 3.

Analogous to the gas cell experiment, the driven and driver sections of the shock tube are connected to vacuum pumps, an agitated mixing tank, and a gas delivery manifold used to barometrically prepare the mixtures for the experimental measurements. The test section of the device has an internal diameter of 10.32 cm, defining the path length L in Eq. (1). Interchangeable ports holding a dynamic pressure transducer (Kistler 601B1) and optical windows circumscribe the test section 2 cm from the shock tube end wall. The pressure transducer records the pressure time history of the incident and reflected shock wave through a charge amplifier (Kistler Type 5018A), and five piezoelectric sensors (Dynasen CA-1135) record the time of arrival of the incident shock wave, from which the incident shock velocity and reflected shock test conditions are determined [56]. When accounting for non-ideal gas dynamics, the uncertainties in reflected shock temperature T_5 and pressure P_5 are typically about 1% [57]. Once the ICL, germanium etalon, and photovoltaic detector were aligned, a series of tests were performed. Example raw voltage data from the detector and transducer charge amplifier, shown in the top of Fig. 4, were recorded at 10 MHz using a PicoScope 4000 series data acquisition module, triggered to record by the time-of-arrival sensors.

Spectrally-resolved CH₄ absorption measurements at 10 kHz were conducted in the shock tube for the temperature range 1050–1610 K and the pressure range 0.4–1.3 atm using scanned-wavelength techniques. For these high-temperature shock tube

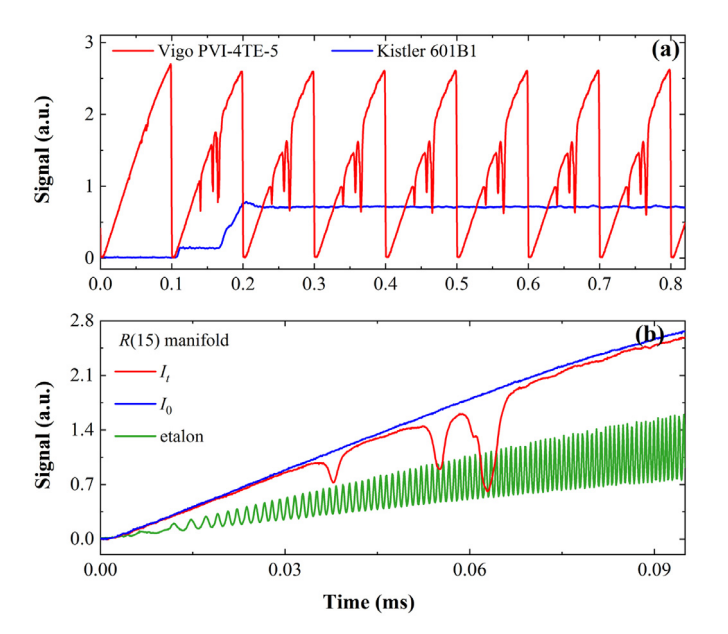


Fig. 4. (a) Raw detector and pressure transducer signals during non-reactive shock heating of CH_4 in a N_2 bath gas. (b) Example scanned-wavelength detector signal in the shock tube for incident light I_0 , transmitted light I_t , and incident light through the etalon.

studies, a mixture of 5% ${\rm CH_4}$ in an ${\rm N_2}$ bath gas was used as the test gas.

4. Results and discussion

Empirically-determined line mixing coefficients of CH₄ perturbed by N₂ are reported for the v_3 R branch between 3024–3200 cm⁻¹ over a range of conditions. Models based on the modified exponential gap (MEG) law and perturbation theory were used to fit the experimental absorbance spectra and determine temperature and pressure dependence of the line mixing parameters. For all spectral modeling and fitting, values for the transition line centers $v_{0,i}$, linestrengths $S_i(T_0)$, lower state energy levels E_i'' and collisional broadening coefficient $\gamma_{air,i}$ were taken from the HITEMP database for CH₄ [23]. Natural abundance of ¹²CH₄ is assumed for all experiments. The following two subsections describe experimental results for the entire v_3 R-branch at high pressures (2–25 atm) and the R(15) manifold at lower pressures (0.2–2 atm), respectively.

4.1. Line mixing in the v₃ R-branch at high pressures

Measured absorbance of the R branch and the best-fit MEG model at a pressure of 24.5 atm at room temperature are shown in Fig. 5(a), with stem plots (blue) showing the positions and linestrengths of the transitions comprising each J-manifold. Each manifold from R(0) to R(18) was fit separately using MEG model with no line mixing considered between different manifolds. Within each manifold, only lines within three orders of magnitude of the strongest line were evaluated for mixing. The line strength of the weakest line included in the line mixing model for each manifold is denoted $S(T_0)_{\min}$ in Table 1. The inset in the topright corner of Fig. 5(a) shows the R(12) manifold absorbance in greater detail, considering 18 transitions. Absorbance from weak lines below the specified linestrength cutoffs was calculated using the HITEMP database parameters assuming Voigt profiles at

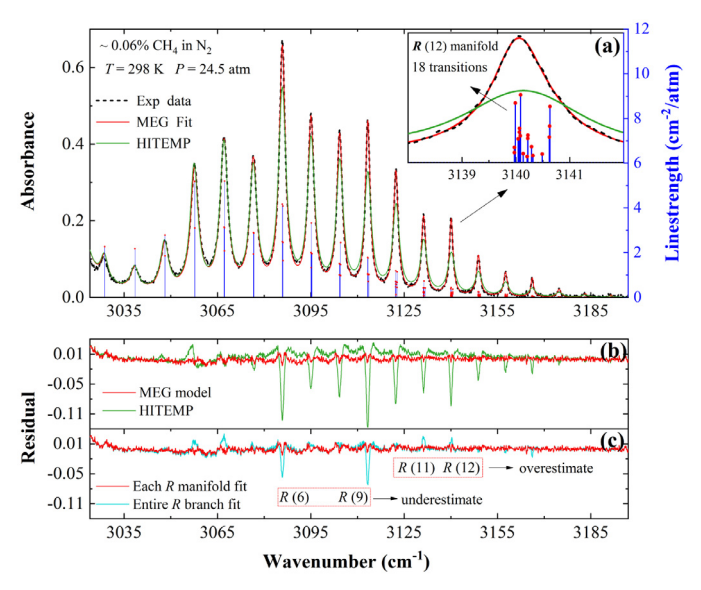


Fig. 5. (a) Measured absorbance for R(0) to R(18) at 24.5 atm and 298 K with corresponding MEG model fits (red) alongside prediction using HITEMP without considering line mixing (green). Note: The air-broadening coefficients and their temperature exponents in HITEMP were used in place of N_2 -broadening. (b) Residuals from the fits considering line mixing (red) and predictions not considering line mixing (green). (c) Residuals from the fits considering line mixing within each manifold individually (red) and considering intra-branch mixing in the entire R branch (blue). (For interpretation of the references to color in this figure legend, the reader is referred to the web version of this article.)

Table 1Temperature-dependent MEG law parameters determined in this work.

J"	$S(T_0)_{\min}$ [cm ⁻² /atm]	No. of lines	a ₁ [10 ⁻³ cm ⁻¹ atm ⁻¹]	a_2	a_3	a_4	$m_{\mathrm{CH_4-N_2}}$
R(4)	2.09 × 10 ⁺⁰	4	0.99 ± 0.03	1.56 ± 0.06	10.00 ± 0.17	2.69 ± 0.15	1.31 ± 0.08
R(5)	$1.95 \times 10^{+0}$	4	$1.32 ~\pm~ 0.01$	$0.94 ~\pm~ 0.02$	$9.99 ~\pm~ 0.04$	$2.69 ~\pm~ 0.15$	$1.35 ~\pm~ 0.02$
R(6)	$1.65 \times 10^{+0}$	6	$1.97 ~\pm~ 0.35$	$0.84 \ \pm \ 0.24$	$10.04 \hspace{.1cm} \pm \hspace{.1cm} 2.68$	$2.69 \hspace{0.1cm} \pm \hspace{0.1cm} 0.15$	$1.98 ~\pm~ 0.18$
R(7)	$1.34 \times 10^{+0}$	6	$1.24 ~\pm~ 0.28$	$0.88 \ \pm \ 0.09$	$10.15 \hspace{.1in} \pm \hspace{.1in} 0.12$	$2.69 \hspace{0.1cm} \pm \hspace{0.1cm} 0.15$	$1.39 ~\pm~ 0.25$
R(8)	9.85×10^{-1}	7	1.22 ± 0.17	$0.86\ \pm\ 0.01$	$10.14 \hspace{.1cm} \pm \hspace{.1cm} 0.08$	$2.69 \hspace{0.1cm} \pm \hspace{0.1cm} 0.15$	1.71 ± 0.15
R(9)	7.09×10^{-1}	8	$2.06 ~\pm~ 0.65$	$0.85 \ \pm \ 0.01$	$9.95 ~\pm~ 1.86$	$2.69 \hspace{0.1cm} \pm \hspace{0.1cm} 0.15$	$1.41 \ \pm \ 0.34$
R(10)	1.22×10^{-1}	11	1.13 ± 0.02	$0.82 \hspace{0.1cm} \pm \hspace{0.1cm} 0.12$	10.43 ± 0.15	$2.69 ~\pm~ 0.15$	1.19 ± 0.02
R(11)	7.49×10^{-2}	13	1.07 ± 0.10	$0.87 \hspace{0.1cm} \pm \hspace{0.1cm} 0.10$	$10.15 \hspace{.1in} \pm \hspace{.1in} 0.02$	2.69 ± 0.15	$1.41 \ \pm \ 0.10$
R(12)	3.87×10^{-2}	18	1.08 ± 0.09	$0.83 \hspace{0.1cm} \pm \hspace{0.1cm} 0.11$	$9.52 \ \pm \ 0.20$	2.69 ± 0.15	1.17 ± 0.09
R(13)	3.10×10^{-2}	14	1.29 ± 0.26	$0.84 \hspace{0.1cm} \pm \hspace{0.1cm} 0.09$	$10.20 \ \pm \ 0.10$	2.69 ± 0.15	$1.24 ~\pm~ 0.22$
R(14)	3.92×10^{-2}	12	1.39 ± 0.33	$0.84 \ \pm \ 0.07$	10.03 ± 0.09	2.69 ± 0.15	$1.34 ~\pm~ 0.26$
R(15)	2.50×10^{-2}	13	1.74 ± 0.54	$0.85 \hspace{0.1cm} \pm \hspace{0.1cm} 0.03$	$9.78 ~\pm~ 0.26$	2.69 ± 0.15	$1.21 \ \pm \ 0.34$
R(16)	1.21×10^{-2}	14	1.21 ± 0.18	$0.84 \hspace{0.1cm} \pm \hspace{0.1cm} 0.06$	10.03 ± 0.13	2.69 ± 0.15	1.20 ± 0.16
R(17)	5.78×10^{-3}	14	1.14 ± 0.02	$0.83 ~\pm~ 0.10$	10.02 ± 0.01	2.69 ± 0.15	$1.31 \ \pm \ 0.02$
R(18)	2.37×10^{-3}	16	$1.19 ~\pm~ 0.05$	$0.84 \ \pm \ 0.05$	10.03 ± 0.13	$2.69 \hspace{0.1cm} \pm \hspace{0.1cm} 0.15$	$1.12 \ \pm \ 0.04$

the gas cell condition; this absorption was fixed in the fitting procedure used to obtain the line mixing parameters of the stronger transitions. For all simulations, the entire spectral range of interest (2850–3200 cm⁻¹) is simulated for each line considered so as to account for absorption by the far wings of each transition.

Comparative residuals from the MEG model fits (red) and from HITEMP predictions not considering line mixing (green) in Fig. 5(b) highlight different levels of line mixing for various R manifolds. The level of disagreement observed by not accounting line mixing (as a percentage of peak manifold absorbance) tends to increase with J'', though not monotonically, associated with the increasing multiplicity of lines within each manifold. The entire R branch was also fit integrally using the MEG model with only one group of line mixing coefficients a_1 through a_4 , with the residuals presented in Fig. 5(c). Considering line mixing amongst all measured spectra captures the line mixing behavior of some J-manifolds very well, such as R(7), R(8) and R(10); however, the line mixing is underestimated for R(6) and R(9) and overestimated for R(4), R(11) and R(12). For the subsequent results reported in this study, each J-manifold was fit independently when using the MEG model.

The R branch was also measured at elevated temperatures, from 541 K to 1021 K at pressures up to 25 atm. Representative absorbance measurements at 10 atm and multiple temperatures are shown in Fig. 6 with the MEG law fits and corresponding residuals. It can be observed that the MEG law model does not fully capture line mixing, with peak residuals ($\sim 4-8\%$) at $T=541~\rm K$ shown in Fig. 6(b), but the model is significantly improved over a HITEMP simulation without line mixing (green). At these elevated temperatures, several hot band transitions are observed, most prominently at 809 K and 1021 K. The measured absorbance in these spectral domains between the fundamental band manifolds is reasonably consistent with expected values calculated using the updated HITEMP database, without accounting for line mixing, and sufficient for properly modeling the far wings of the primary manifolds of interest. We note that transitions of the naturally abundant ($\sim 1\%$) ¹³CH₄ are also included in the absorbance simulations, although no line mixing is accounted here due to the relative weakness of these lines being below the aforementioned linestrength threshold. Similarly, the fit provided by the MEG model at the highest pressure of 25 atm (and for these elevated temperatures) generally captures the line mixing behavior, although there remains small underestimation of peak absorbance in each manifold with peak residuals of ~ 0.8-5.6% at T = 541 K and ~ 4.9-10.6% at T = 1021 K.

The species-specific MEG law coefficients a_2 , a_3 , and a_4 for each J-manifold are obtained by fitting the absorbance at a single condition where the model works very well (room temperature and

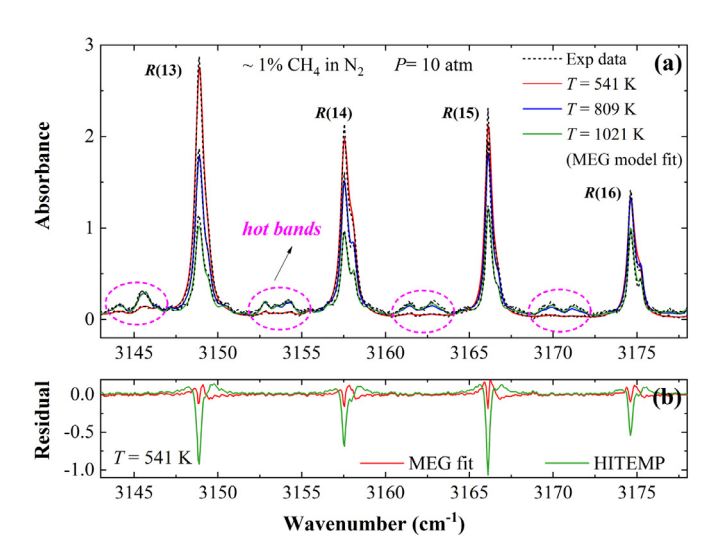


Fig. 6. (a) Measured absorbance from R(13) to R(18) for elevated temperatures (541 K, 809 K and 1021 K) at 10 atm with corresponding spectral fits from the MEG law model. Note: The air-broadening coefficients and their temperature exponents in HITEMP were used in place of N_2 -broadening. (b) Residuals from the fits considering line mixing (red) and predictions without considering line mixing (green) at 541 K. (For interpretation of the references to color in this figure legend, the reader is referred to the web version of this article.)

25 atm) [28], and are held constant when fitting the spectra at different temperatures to obtain $a_1(T)$. The temperature dependence of $a_1(T)$ for each manifold was determined by applying a weighted least-squares fit [58] of the power-law expression in Eq. (20) to these $a_1(T)$ values at different temperatures (also at 25 atm). Representative experimentally obtained values of $a_1(T)$ for the R(14), R(15) and R(17) manifolds are presented alongside corresponding power-law fits in Fig. 7. The calculated species-specific MEG law coefficients and temperature exponents for all the manifolds are given in Table 1, along with the number of lines considered in the fits and the minimum transition linestrength among those lines, $S(T_0)_{\min}$. Overall weaker absorbance in the v_3 band at elevated temperatures contributes to increased measurement uncertainty in the coefficients as seen in Fig. 7, largely due to lower measurement signal-to-noise ratio (SNR). Although inter-manifold blending is present in the spectral regions surrounding the higher I" manifolds, the restriction to intra-manifold line mixing (similar E'' at the same J'') in our fitting procedure enables improved spectral simulation compared to a single MEG model for the entire branch. As such, the listed coefficients for each manifold in Table 1 are

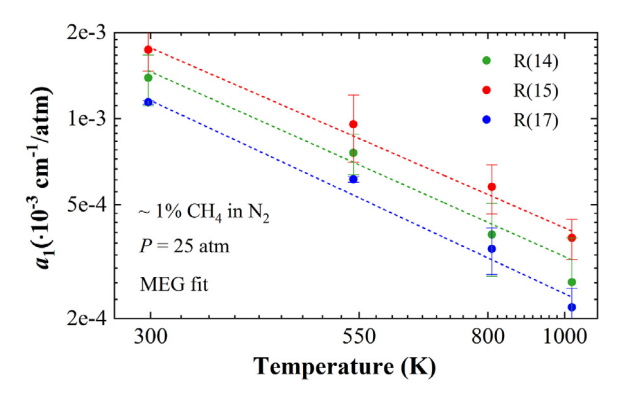


Fig. 7. Temperature dependence of the line mixing coefficients a_1 [cm⁻¹/atm] and power law fits for the manifolds R(14), R(15) and R(17) at the pressure of 25 atm. The temperature-dependent parameters for the other manifolds are given in Table 1

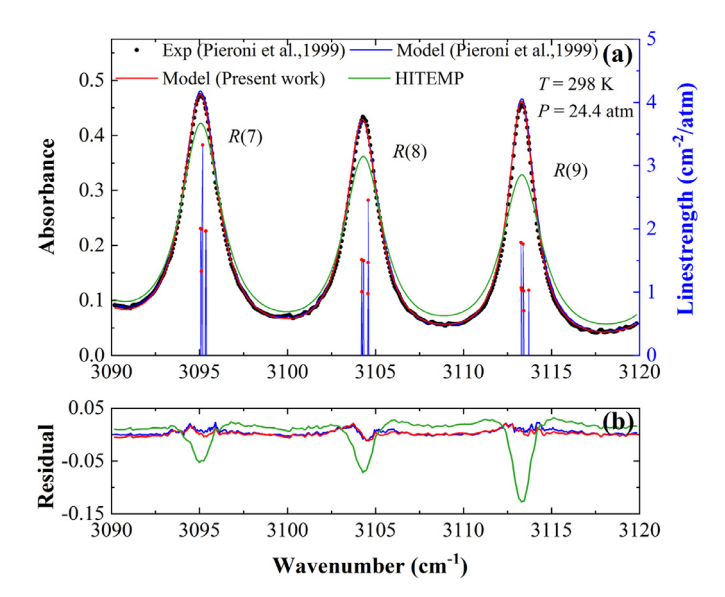


Fig. 8. (a) Absorbance (X = 0.0006, L = 9.4 cm) calculated from $\alpha/P_{\rm CH_4}$ [cm⁻¹/atm] reported by Pieroni et al [28] at P = 24.4 atm and ambient temperature for R(7)–R(9). Measured values (black points) shown alongside calculations [28] (blue), the MEG law model of the present work (red), and predictions without line mixing (green). Note: The air-broadening coefficients and their temperature exponents in HITEMP were used in place of N₂-broadening in the present work, while the N₂-broadening was deduced by multiplying the air-broadening in HITRAN by a factor of 1.02 [28,34]. (b) Residuals from the two line mixing models and calculations without line mixing. (For interpretation of the references to color in this figure legend, the reader is referred to the web version of this article.)

valid for transitions with the same J''. It should be noted that only manifolds for which line mixing is significant, R(4)–R(18), are included in Table 1. R(0) only has one transition, and the line mixing within R(1)–R(3) is either restricted by transition symmetries (A, E, or F) or very weak ($a_1(T_0) < 10^{-14}$ cm⁻¹/atm).

To test the validity of the empirical MEG model, the reported coefficients were used to calculate the absorbance at P=24.4 atm and T=298 K for comparison with the measured and calculated results from Pieroni et al [28] as shown in Fig. 8. The spectrally-resolved absorption coefficient ($\alpha/P_{\rm CH_4}$ [cm⁻¹/atm]) for the wavenumber region reported in that study was multiplied by the partial pressure of CH₄ and the pathlength of the present experiments to obtain a comparable spectral absorbance α_{ν} . The predicted spectrum from the MEG law-based line mixing model in the present work is in very good agreement with the absorbance measured by Pieroni et al [28] and shows consistent accuracy in capturing the effects of line mixing among the various manifolds.

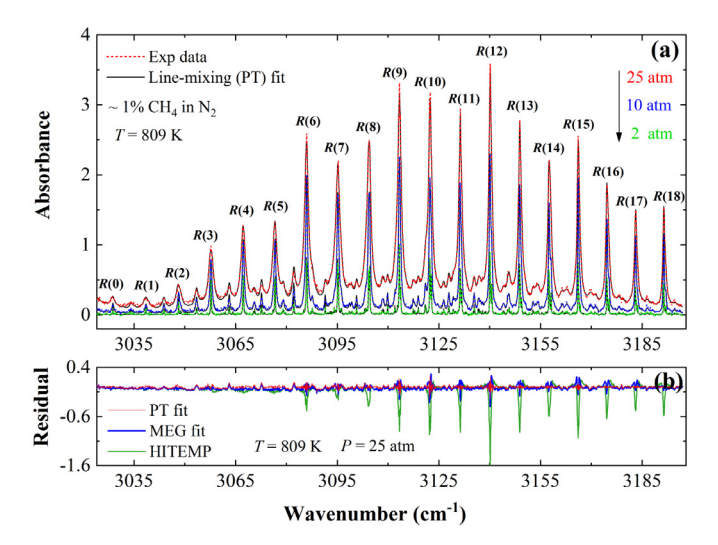


Fig. 9. (a) Measured absorbance from R(0) to R(18) at various pressures (2 atm, 10 atm and 25 atm) at 809 K with corresponding best-fits using first-order line mixing with the Voigt profile (red). Note: The air-broadening coefficients and their temperature exponents in HITEMP were used in place of N_2 -broadening. (b) Residuals from the fits of the first-order line mixing model (red), MEG law model (blue) and predictions without considering line mixing (green) at 25 atm. (For interpretation of the references to color in this figure legend, the reader is referred to the web version of this article.)

Fig. 9 (a) shows the broader R-branch spectra (R(0)-R(18)) measured at 809 K for varying pressure, alongside corresponding spectral fits of the first-order line mixing model (PT) using the Voigt profile. The residuals for both the PT model (red) and MEG law (blue) are shown in Fig. 9(b). While the MEG model produces larger residuals as pressure or gas density decreases, the first-order line mixing model derived from perturbation theory could fit the measured absorbance well at any pressure and temperature. However, this good agreement associated with the PT model fit should not necessarily be interpreted as a more physical representation of line mixing, but rather the simple result of many more free parameters. In perturbative treatment theory, Eq. (11) is only valid when the transition overlap is not severe [41]; strongly overlapping lines in the measured high-pressure FTIR spectra convolute the retrieved Y_i values obtained from the PT model fits such that they lose direct relation to the off-diagonal elements in the relaxation matrix and allow for multiple solutions. This convolution may be acutely pronounced for the high J'' R-manifolds, wherein more lines exist and line mixing effects are more significant. In floating the Y_i values over the range of high pressures (~ 5-25 atm) there was no clear pressure dependence (as would be expected) of the line mixing coefficients obtained from the PT model fit, with the exception of the R(2)–R(4) manifolds (owing to fewer lines in each manifold). Multiple solutions to the PT fit could also be found given the large number free parameters and fewer distinct spectral features at elevated pressures. As such, a higher-resolution lower-pressure study was deemed necessary for utilization of perturbation theory.

4.2. Line mixing of the R(15) manifold transitions

A detailed high spectral-resolution investigation of line mixing among the 13 transitions comprising the R(15) manifold was conducted using interband cascade laser absorption spectroscopy near 3.16 μ m at various pressures from 0.3 atm to 2.0 atm in the heated gas cell and shock tube. Fig. 10 highlights the transitions comprising the R(15) manifold along with their ground-state symmetries C''(A, E, F). The transitions can be grouped into three clusters, referenced by their left-to-right ordering in Fig. 10. Line mixing between the first and second cluster is observed at pressures as low

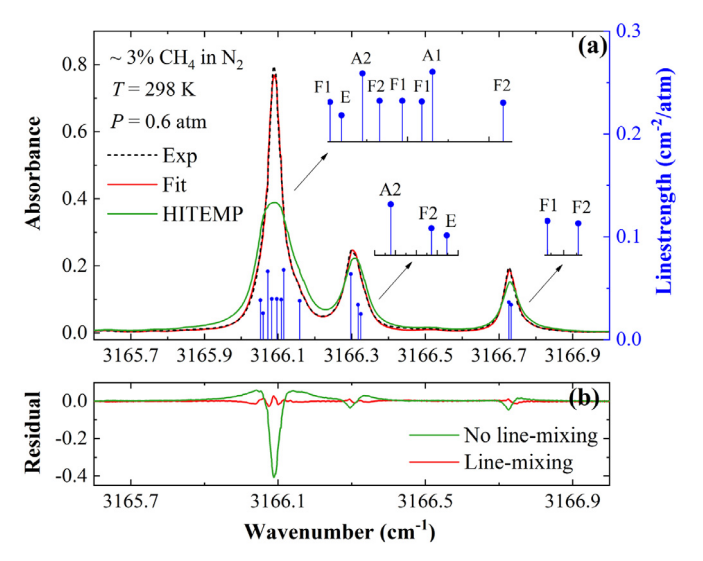


Fig. 10. (a) Measured absorbance of the R(15) manifold at ambient temperature and 0.6 atm with corresponding best-fits from the PT-based line mixing model using the Voigt lineshape profile (red) alongside prediction using HITEMP without considering line mixing (green). The stem plots indicate the symmetries of each transition. Note: The air-broadening coefficients and their temperature exponents in HITEMP were used in place of N_2 -broadening. (b) Residuals from the best-fit of the line mixing model and predictions without considering line mixing. (For interpretation of the references to color in this figure legend, the reader is referred to the web version of this article.)

as 0.6 atm, while line mixing between the third cluster and the other two clusters is relatively weak, and we show in this study that it can be neglected at pressures lower than 2 atm. The weak line mixing contribution by the third cluster is likely due to its relative spectral isolation [31], resulting in the constituent transitions with F_1 and F_2 symmetries following the sum rule independent of the other R(15) transitions at each pressure.

4.2.1. Line mixing and lineshape model performance

The MEG model and the PT-based model were both used to fit the experimental laser absorption data, and Fig. 11(a) shows the measured absorbance alongside the best-fits from each model, with residuals shown in the lower panel. As expected from the FTIR study, the MEG model does not fully capture line mixing at these low pressures, and the resulting fits yield peak residuals of 5%-30%. The PT-based model, however, better captures line mixing in the R(15) manifold, yielding peak residuals less than 5.5% at any pressure. To examine the performance of the different line mixing models at different temperatures and pressures in more detail, the root mean square error (RMSE) was calculated from the bestfit residuals for both models, as shown in Fig. 12. The RMSE for the MEG model decreases with pressure, while there is no obvious trend for the RMSE obtained from the PT-based model, though the values are smaller for pressures lower than 1 atm. Fig. 12(b) shows that the performance of each model is not strongly dependent on temperature for the temperature range considered in this study, though the first order PT-based model outperforms the MEG model at all temperatures and pressures. The R(15) manifold appears to demonstrate high selectivity in collisional effects for the examined pressure range; significant coupling among the F_1 and F_2 transitions is apparent in the first (strongest) cluster, while much less significant coupling is evident in the third (weakest) cluster. This selectivity renders statistically based fitting laws such as MEG model inappropriate for characterizing line mixing in CH₄ spectra [28], especially at low pressures. For this reason, the remaining discussion focuses on the results obtained from the first order PT-based line mixing model.

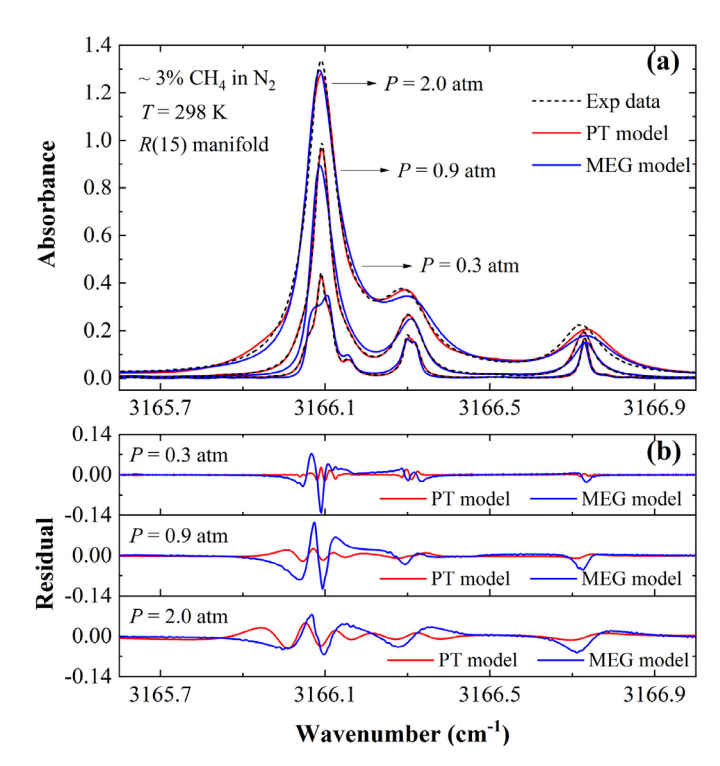


Fig. 11. (a) Measured absorbance of the R(15) manifold for various pressures (0.3 atm, 0.9 atm and 2.0 atm) at ambient temperature (298 K) with corresponding best-fits from the first-order Line mixing Voigt profile (red) and MEG model (blue). Note: The air-broadening coefficients and their temperature exponents in HITEMP were used in place of N_2 -broadening. (b) Residuals from the best-fit of two line mixing models for each pressure. (For interpretation of the references to color in this figure legend, the reader is referred to the web version of this article.)

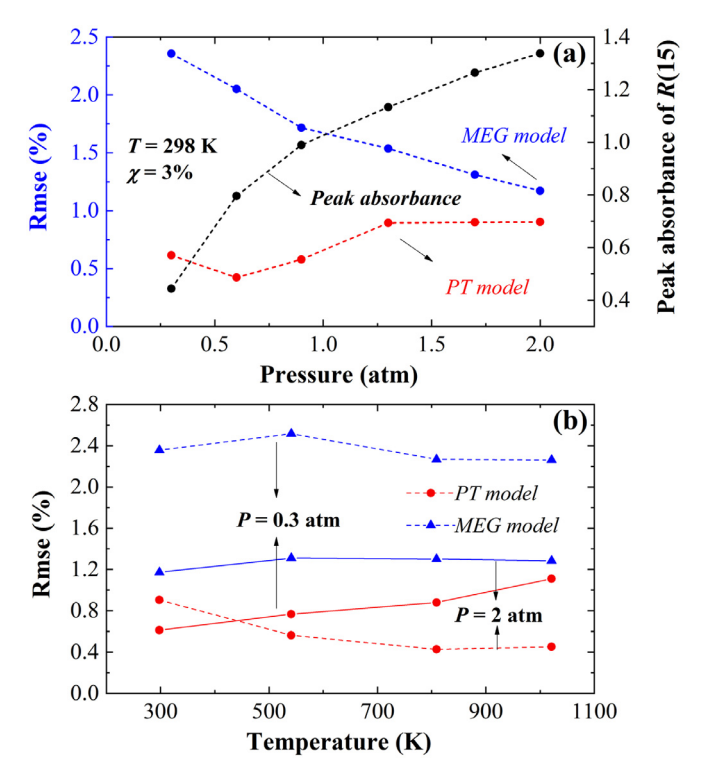


Fig. 12. (a) Root mean square error (RMSE) from the best-fits of the PT model and the MEG model at pressures from 0.3 atm to 2.0 atm at ambient temperature. (b) RMSE from the best-fits of the PT model and the MEG model at various temperatures (298 K, 541 K, 809 K and 1021 K) at 0.3 atm and 2.0 atm. RMSE calculated as % of the peak absorbance.

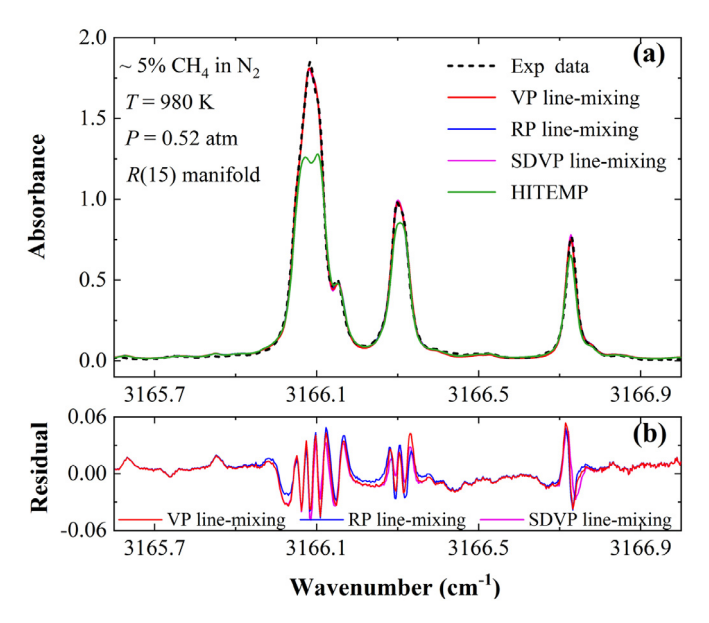


Fig. 13. (a) Measured absorbance of the R(15) manifold at 980 K and 0.52 atm with corresponding best-fits from the first order line mixing model using Voigt, Rautian and speed-dependent lineshape profiles. Note: The air-broadening coefficients and their temperature exponents in HITEMP were used in place of N_2 -broadening. (b) Residuals from the best-fit of the three models.

To confirm the appropriateness of the Voigt lineshape profile for this study, the first-order PT-based line mixing model using Rautian and speed-dependent profiles were also spectrally fitted against the experimentally measured absorbance at low pressures (\leq 2 atm). Fig. 13 shows the best fits and fitting residuals for the first-order model with the three profiles at 0.52 atm and 980 K with a Lorentz-to-Doppler broadening ratio of 2.8.

The RSME decreases from 1.23×10^{-2} for the original Voigt lineshape profile (VP) to 1.17×10^{-2} for the Rautian profile (RP) and 1.15×10^{-2} for the speed-dependent Voigt profile (SDVP). The inclusion of Dicke narrowing or speed dependence yielded little improvement, and the retrieved corresponding narrowing coefficients approach zero for the two profiles in most cases. For this reason, the Dicke narrowing and speed-dependent coefficients were not measured in this study, and we report only the line mixing coefficients obtained using the Voigt lineshape profile in subsequent plots and in Table 2. We note that collisional widths were calculated using data from HITEMP [23] instead of assigning them as free parameters when using the first-order line mixing profiles [30,37] owing to unreliable fitting of a highly underdetermined system with significant line mixing effects.

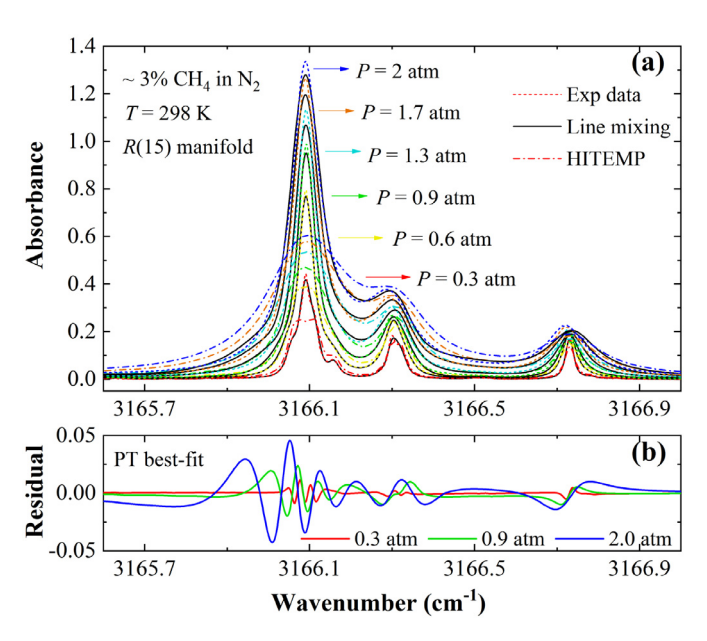


Fig. 14. (a) Measured absorbance in the R(15) manifold from 0.3 atm to 2 atm at 298 K with corresponding best-fits from the first-order line mixing model using the Voigt profile. Predicted absorbance using HITEMP (not considering line mixing) also shown for reference. Note: The air-broadening coefficients and their temperature exponents in HITEMP were used in place of N_2 -broadening. (b) Residuals for the pressures of 0.3 atm, 0.9 atm and 2.0 atm.

4.2.2. Temperature-dependent line mixing in R(15)

The first-order PT-based model using the Voigt profile was spectrally fitted against the measured absorbance of the R(15)manifold at ambient temperature from 0.3-2 atm, as shown in Fig. 14 alongside HITEMP predictions (not considering line mixing) for reference. Overall, we observe that line mixing in the R(15)manifold is significant, even at the lowest pressure condition examined, typically resulting in a factor of two or more increase in the peak linecenter absorbance for the strongest line cluster. Calculations reveal that the collisional width is larger than the frequency spacing at pressures greater than 0.2 atm, associated with population transfers between the same rotational energy states with different levels α (where α is an integer corresponding to different levels of the same rotational quanta) [54]. The R(15) manifold absorption was also measured in the heated gas cell at 541 K, 809 K and 1021 K, and fit with the first-order PT-based model using the Voigt lineshape profile, as shown in Fig. 15. Similar to the room temperature results, the first-order line mixing model is shown to capture the spectra well at these higher temperatures, yielding low residuals near 3%. Line mixing coefficients at temperatures higher

Table 2 Measured first-order line mixing coefficient and temperature dependence for CH_4 R(15) manifold.

J' C' α'	J" C" α"	ν [cm ⁻¹]	Y _i (0.3 atm) [no unit]	Y _i (0.6 atm) [no unit]	Y _i (1.3 atm) [no unit]	Y _i (2.0 atm) [no unit]	$n_{\mathrm{CH_4-N_2}}$
16 F ₂ 57	15 F ₁ 3	3166.05235	0.05 ± 0.02	-0.43 ± 0.06	-27.39 ± 0.70	-112.83 ± 2.81	3.48 ± 0.12
16 E 38	15 E 2	3166.05948	-0.54 ± 0.04	-2.20 ± 0.11	2.49 ± 0.48	14.00 ± 0.30	$0.49 ~\pm~ 0.07$
16 A ₁ 21	15 A ₂ 2	3166.07227	0.46 ± 0.03	-3.10 ± 0.10	-64.08 ± 2.31	-536.66 ± 15.75	$3.41 ~\pm~ 0.07$
16 F ₁ 57	15 F ₂ 4	3166.08286	4.38 ± 0.06	31.88 ± 0.30	457.90 ± 10.32	3185.10 ± 73.80	$2.54 ~\pm~ 0.03$
16 F ₂ 58	$15 F_1 4$	3166.09674	-4.29 ± 0.07	-26.99 ± 0.45	-446.09 ± 10.00	-3178.60 ± 73.48	$2.54 ~\pm~ 0.03$
16 F ₂ 56	15 F_1 2	3166.10877	$0.73 \hspace{1mm} \pm \hspace{1mm} 0.06$	1.00 ± 0.31	16.73 ± 1.18	118.39 ± 2.36	$3.53 ~\pm~ 0.40$
16 A ₂ 18	15 A ₁ 1	3166.11530	-0.72 ± 0.03	2.17 ± 0.10	61.75 ± 2.26	526.22 ± 15.39	$4.37 \ \pm \ 0.07$
16 F ₁ 56	$15 F_2 3$	3166.15875	-0.03 ± 0.01	-0.30 ± 0.03	-1.26 ± 0.44	-25.41 ± 2.20	$1.68 ~\pm~ 0.17$
16 A ₁ 20	15 A ₂ 1	3166.29768	0.28 ± 0.01	0.91 ± 0.04	1.01 ± 0.03	1.17 ± 0.03	$1.48 ~\pm~ 0.06$
16 F ₁ 55	15 F ₂ 2	3166.31721	-0.96 ± 0.22	-3.74 ± 0.43	-0.23 ± 0.02	14.92 ± 0.53	$1.05 ~\pm~ 0.17$
16 E 37	15 E 1	3166.32460	$0.55 ~\pm~ 0.04$	2.27 ± 0.11	-2.56 ± 0.50	-14.44 ± 0.31	$0.49 ~\pm~ 0.07$
16 F ₂ 55	15 F_1 1	3166.72679	$1.38 ~\pm~ 0.03$	$2.62 ~\pm~ 0.06$	6.95 ± 0.13	9.63 ± 0.37	$2.23\ \pm\ 0.04$
16 F ₁ 54	15 F ₂ 1	3166.73280	$\text{-}1.50 \hspace{0.1cm} \pm \hspace{0.1cm} 0.04$	$-2.84 \ \pm \ 0.07$	$-7.51 ~\pm~ 0.15$	$\textbf{-10.42} \ \pm \ \textbf{0.44}$	$2.23\ \pm\ 0.04$

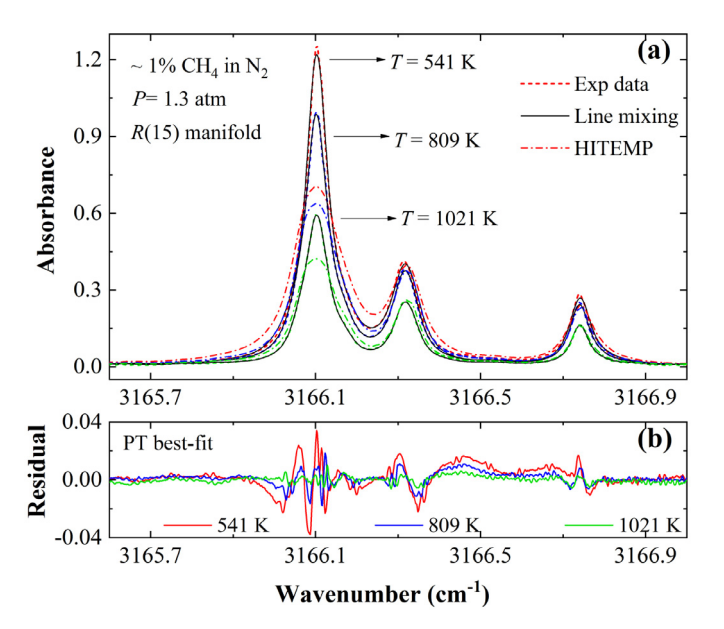


Fig. 15. (a) Measured absorbance of the R(15) manifold at 541 K, 809 K and 1021 K and 1.3 atm with corresponding best-fits from the first-order line mixing model using the Voigt profile. Predicted absorbance using HITEMP (not considering line mixing) also shown for reference. Note: The air-broadening coefficients and their temperature exponents in HITEMP were used in place of N_2 -broadening. (b) Residuals from the fits to the experimental data at each temperature.

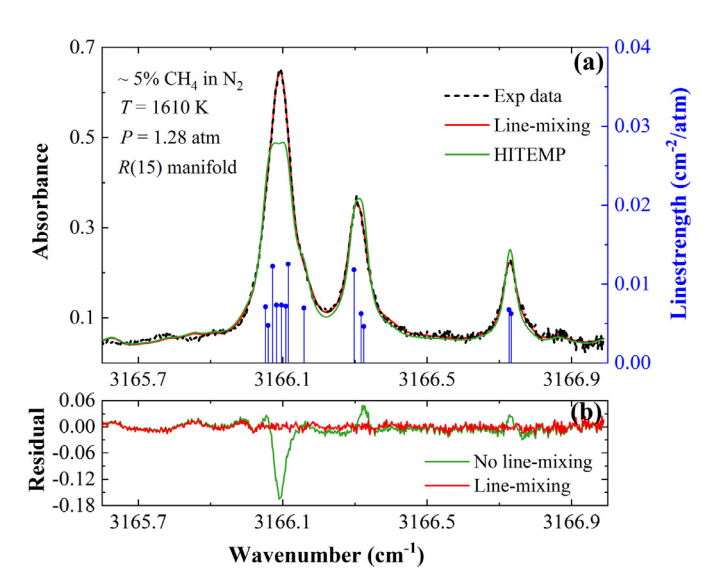


Fig. 16. (a) Measured absorbance of the *R*(15) manifold at 1610 K and 1.28 atm with corresponding best-fits from the first order line mixing model using the Voigt lineshape profile. Predicted absorbance using HITEMP (not considering line mixing) is shown for reference. Note: The air-broadening coefficients and their temperature exponents in HITEMP were used in place of N₂-broadening. (b) Residuals from the fits with line mixing and calculations without line mixing.

than 1050 K were measured in the shock tube. A representative measured absorbance and best-fit first-order line mixing model at 1610 K are shown in Fig. 16 with a simulation not accounting line mixing for reference.

An examination of the line mixing contributions by specific transitions, designated by C'' $\alpha'' \rightarrow \alpha'$, reveal notable differences among the clusters comprising the R(15) manifold. The pressure dependencies of the line mixing coefficients obtained by the first-order PT model are displayed in Fig. 17 with polynomial fits for the transitions spanning $\nu = 3166.05$ cm⁻¹ to 3166.16 cm⁻¹ in Fig. 17(a) and linear fits for the F_1 1 \rightarrow 55 (3166.727 cm⁻¹)

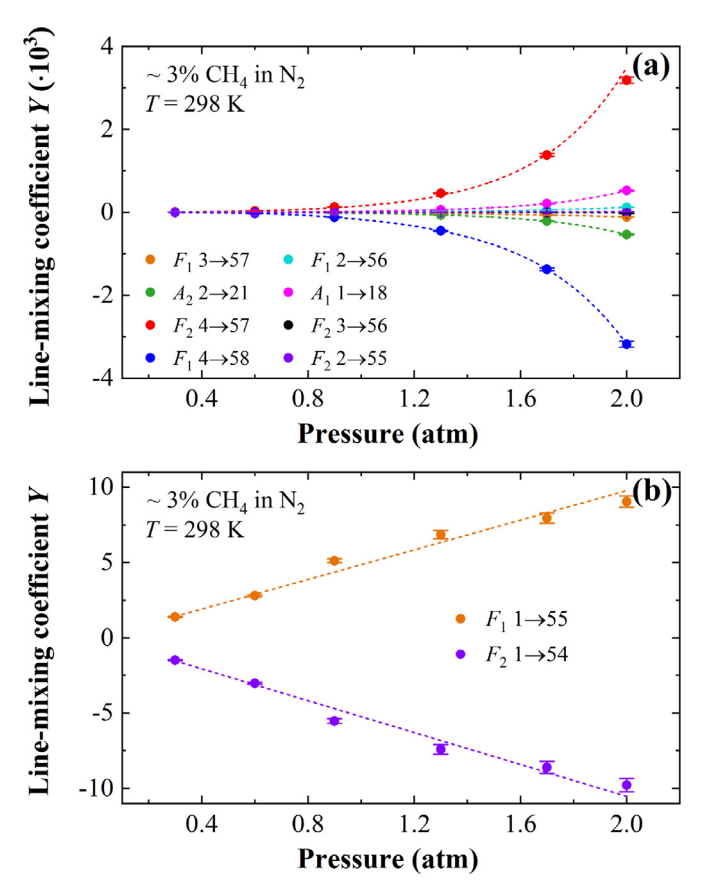


Fig. 17. Pressure dependence of the measured line mixing parameter Y_i given by the first order model using the Voigt profile for the transitions (a) spanning 3166.052 cm⁻¹ to 3166.158 cm⁻¹. (b) F_1 1 \rightarrow 55 at 3166.727 cm⁻¹ and F_2 1 \rightarrow 54 at 3166.733 cm⁻¹. Here, T_1 = 298 K and the pressures from 0.3 atm to 2.0 atm.

and F_2 1 \rightarrow 54 (3166.733 cm⁻¹) transitions in Fig. 17(b). The line mixing coefficients increase dramatically as pressure increases, reaching 10^3 for the F_2 4 \rightarrow 57 (3166.08 cm⁻¹) and F_2 4 \rightarrow 58 (3166.10 cm⁻¹) transitions while the coefficients are approximately linear with pressure for the F_1 1 \rightarrow 55 (3166.727 cm⁻¹) and F_2 1 \rightarrow 54 (3166.733 cm⁻¹) transitions, achieving a much smaller magnitude. The pressure dependence of the line mixing coefficients at 1021 K is depicted in Fig. 18(a), demonstrating a nominal decrease and more linear dependence on pressures compared with the values at ambient temperature. In general, the line mixing coefficients with smaller magnitudes have a more linear pressure dependence, consistent with the approximation of the relaxation matrix in the first-order line mixing model based on perturbation theory; however, Eq. (11) does not appear valid in this regime, since the coefficients with larger magnitudes increase significantly and nonlinearly with pressure.

To check that the non-linear pressure dependence of the mixing coefficients was a not an issue of over-fitting too many free parameters, a multispectrum fitting routine [25] was used to fit the spectra over a range of pressures from 0.3 atm to 2.0 atm, constraining the pressure dependence of the line mixing coefficients, with units of [atm $^{-1}$], to be strictly linear. However, the absorbance spectrum at each pressure could not be fit well, yielding peak residuals typically larger than 10%, reaching 20% at the lowest measured pressure of 0.3 atm. The nonlinear dependence of Y_i parameters on pressure is similar to the Dicke narrowing coefficients in Rautian and Galatry profiles [59,60] with the growth rate increasing with increasing pressure. The retrieved Dicke narrowing coefficients also deviate from the dynamic friction coefficients due to the neglect

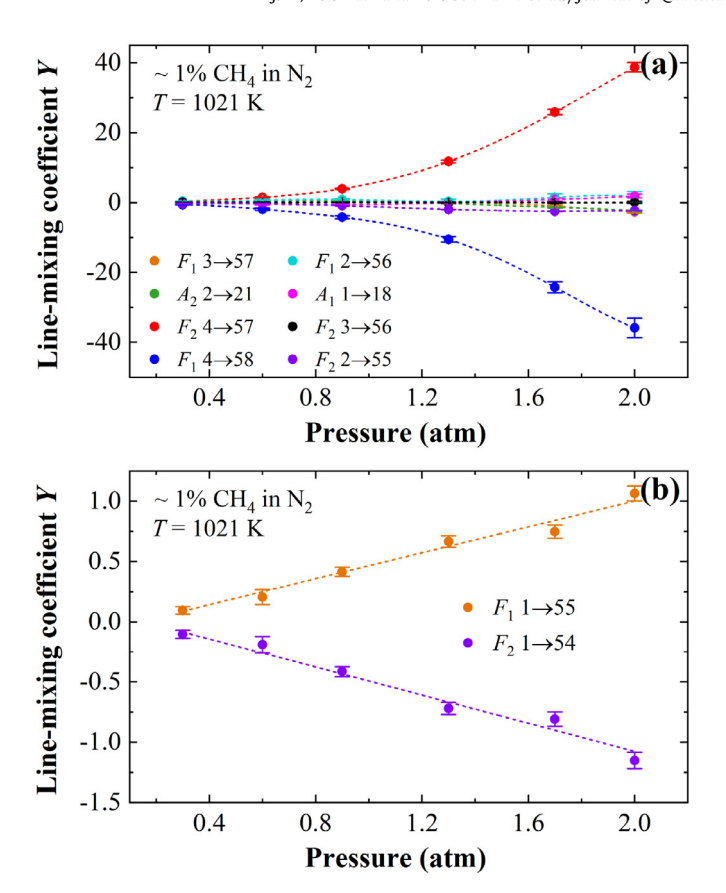


Fig. 18. Pressure dependence of the measured line mixing parameter Y_i given by the first order model using Voigt profile for the transitions (a) spanning 3166.052 cm⁻¹ to 3166.158 cm⁻¹. (b) F_1 1 \rightarrow 55 at 3166.727 cm⁻¹ and F_2 1 \rightarrow 54 at 3166.733 cm⁻¹. Here, T=1021 K and the pressures from 0.3 atm to 2.0 atm.

of the correlations between velocity-changing and state-changing collisions [61], which is similar to the deviation between the measured Y_i parameters and the values calculated by Eq. (11). Thus, a line mixing model based on first-order perturbation theory may not be sufficient to physically characterize the transitions exhibiting this nonlinear mixing behavior with increasing pressure, and a higher-order line mixing model may better describe the observed trends. Nonetheless, a modified first-order PT-based model (allowing for some non-linearity of Y_i parameters with pressure) captures the CH₄ line mixing satisfactorily, and may be more simply used as an empirical approach (as opposed to a higher order model) to simulate the spectra over a range of conditions, despite potential non-physicality.

These results may be further examined in the context of previous line mixing studies. The line mixing coefficients in the R(15)manifold are observed to be relatively large, achieving values up to ~4.4 at 0.3 atm. These values are much greater than those in the lower J-manifolds, such as those measured by Ghysels et al [37], who observed a maximum line mixing coefficient of 0.5 among the transitions comprising the R(6) manifold at atmospheric pressure and ambient temperature. Significant line mixing effects among the transitions comprising high-J" manifolds (J" > 15)-such as R(17) and R(19)—have also been documented by Grivoriev et al [32], who noted that the absorbance predicted by the summation of isolated lines underestimated the experimentally measured value by a factor of 2, similar to the results for the R(15) manifold. The authors cautioned that the Y_i parameters obtained in the fit were unlikely to be reliable, despite that the calculated and observed absorbance were in good agreement [32]. Unlike the current

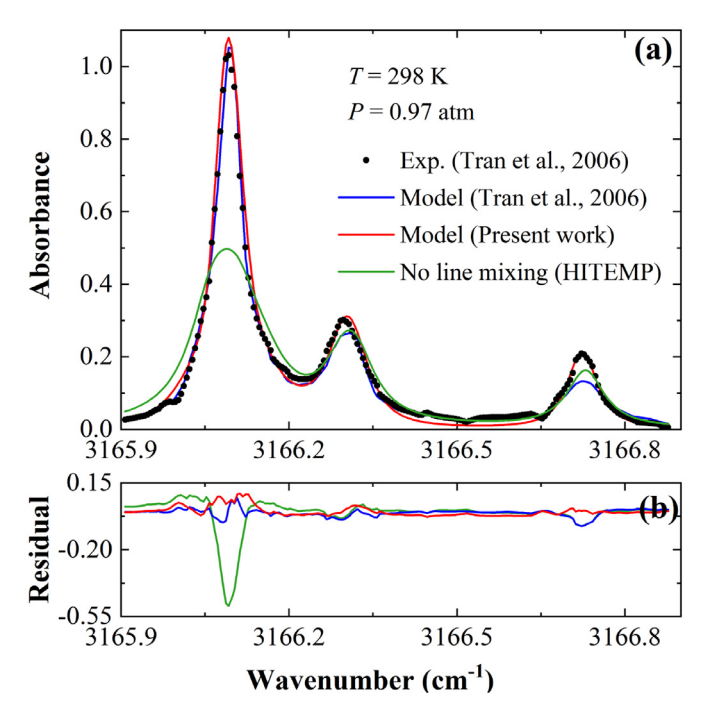


Fig. 19. (a) Absorbance (X = 0.03, L = 9.4 cm) calculated from the absorption coefficient α/P_{CH_4} (cm⁻¹/atm) reported by Tran et al [34] at P = 0.97 atm and ambient temperature for R(15). Measured values (black points) shown alongside calculations by the model of Tran et al [34] (blue), the first-order model in the present work (red), and calculated values without line mixing (green). Note: The air-broadening coefficients and their temperature exponents in HITEMP were used in place of N_2 -broadening in the present work while the N_2 -broadening was deduced by multiplying the air-broadening in HITRAN by a factor of 1.02 [28,34]. (b) Residuals from the two line mixing models and calculations without line mixing. (For interpretation of the references to color in this figure legend, the reader is referred to the web version of this article.)

work, no pressure or temperature dependence was investigated, precluding more detailed comparison beyond ambient conditions.

For the current work capturing the R(15) manifold, Y_i parameters with their uncertainties at the pressures 0.3, 0.6, 1.3 and 2.0 atm are presented in Table 2. The listed uncertainties for each parameter are calculated according to the methods detailed in Appendix A. A polynomial fit may be implemented to describe the pressure dependence of Y_i , so that the parameters at pressures other than those listed in Table 2 can also be obtained. The temperature dependence exponent n in Eq. (20) for each line mixing parameter Y_i was determined by a power-law fit, using the Y_i parameters evaluated at atmospheric pressure. These empirical relationships readily enable calculation of spectrally-resolved absorbance in the R(15) manifold for broader CH_4 sensing applications.

To test the validity of the empirical model, the line mixing parameters were used to calculate the absorbance at P=0.97 atm and T=298 K for comparison with the measured and calculated results from Tran et al [34] as shown in Fig. 19. As with the literature comparison for the MEG law coefficients, the spectrally-resolved absorption coefficient ($\alpha/P_{\rm CH_4}$ [cm $^{-1}/{\rm atm}$]) for R(15) reported in that study was multiplied by the partial pressure of CH₄ and the pathlength of the experiments in the present investigation to obtain a comparable spectral absorbance α_{ν} . As no experiments were conducted at exactly 0.97 atm in this study, the Y_i parameters for P=0.97 atm were obtained using a 3-order polynomial fit of the parameters with respect to pressure at ambient temperature in Table 2. Graphical depictions of the polynomial fits used to obtain Y_i at 0.97 atm are shown in Fig. 17. The predicted spectrum from the first-order line mixing model in the present work

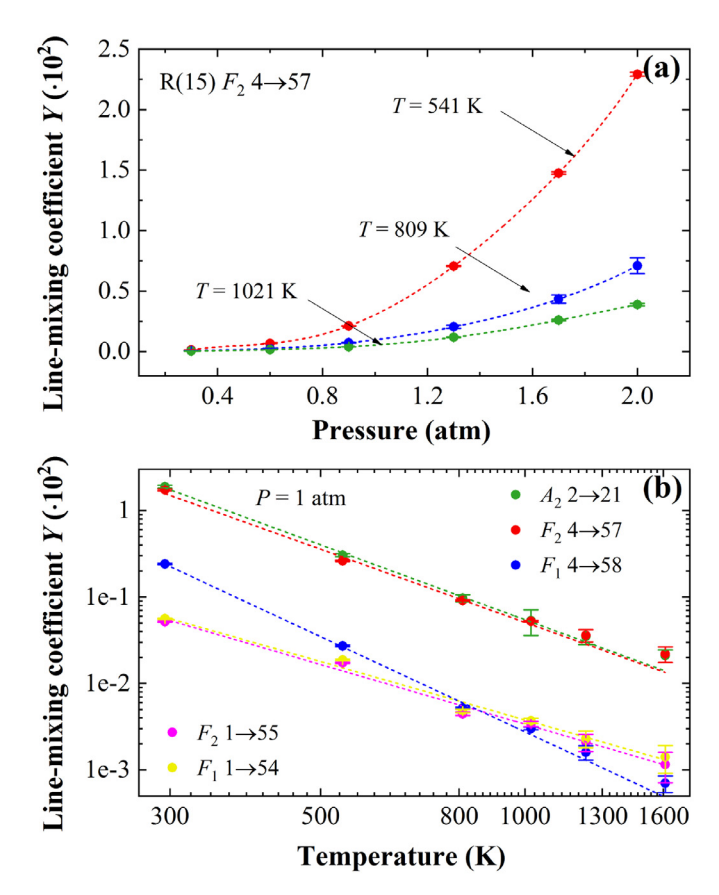


Fig. 20. (a) Pressure dependence of the line mixing parameter Y_i for the F_2 4 \rightarrow 57 transition at various temperatures (298 K, 541 K, 809 K, 1021 K). (b) Temperature dependence of the line mixing coefficients Y and power law fits for transitions (A_2 2 \rightarrow 21, F_2 4 \rightarrow 57, F_1 4 \rightarrow 58, F_2 1 \rightarrow 55, F_1 1 \rightarrow 54) in the R(15) manifold at 1 atm.

is in good agreement with the absorbance measured by Tran et al [34] and shows some improved accuracy in capturing the effects of line mixing among the F_1 1 \rightarrow 55 (3166.727 cm $^{-1}$) and F_2 1 \rightarrow 54 (3166.733 cm $^{-1}$) transitions relative to the model presented in that study. It should be noted that the prior work was using an older and more sparse database. As expected, both models show much better agreement than the prediction which does not consider line mixing near the most prominent cluster of lines.

Finally, we examine the temperature dependence of the firstorder PT-based model for the transitions comprising the R(15)manifold based on data from both the heated gas cell and shock tube experiments. Fig. 20(a) shows the line mixing coefficient for the prominent F_2 4 \rightarrow 57 transition near 3166.083 cm⁻¹ at the temperatures 541 K, 809 K and 1021 K over the range of pressures studied. The magnitudes of the line mixing coefficients for this transition and the others decrease dramatically with increasing temperature, exhibiting a more approximately linear pressure dependence. Fig. 20(b) shows the line mixing coefficients determined at different temperatures spanning 298 K to 1610 K at P=1 atm for several representative transitions in the R(15) manifold. As discussed previously, the Y_i coefficients were fit with a power law using Eq. (20) to obtain the temperature-dependent exponent n for each transition, and the resulting fits are also plotted in Fig. 20(b). The power law formulation captures the temperature dependence of the line mixing coefficients reasonably well, demonstrating its applicability for predicting CH₄ spectra across a wide range of temperatures. The temperature-dependent exponent n determined at atmospheric pressure for each transition is listed in Table 2 along with associated uncertainties calculated according to the methods detailed in Appendix A.

5. Conclusion

Empirically-derived line mixing parameters and associated temperature-dependence exponents are reported for the R branch of the v_3 band of CH₄ perturbed by N₂ in the 3024–3200 cm⁻¹ region. Experiments were conducted over a wide range of temperatures from 300 K to 1600 K, utilizing a heated gas cell and a shock tube facility. High-temperature experiments were coupled with an FTIR survey of the R-branch from 2-25 atm and a more focused laser absorption spectroscopy investigation of the R(15) manifold at lower pressures. Two empirical models were tested and found appropriate for different ranges of gas density. A modified exponential gap (MEG) law, with manifold-specific coefficients, was found to capture line mixing in the R branch manifolds from R(0) to R(18) with very good accuracy at the higher pressures (< 3% max residual at 25 atm) and increased error with decreasing pressure and gas density. Despite residual error, the MEG law model offers significant improvement over conventional modeling that neglects line mixing and reasonable agreement down to 2 atm, with temperature scalability to 1020 K. Line mixing of the R(15) manifold was examined at lower pressures of 0.3–2 atm and at higher temperatures up to 1610 K using a narrow-band interband cascade laser. A first-order line mixing model based on perturbative treatment theory was developed to improve spectral simulation and scaling with temperature and pressure compared to the MEG law. The temperature dependence of the PT model coefficients follows the power law while the pressure dependence is nonlinear for some transitions in R(15), and requires interpolation between pressure-specific coefficients for scaling. In aggregate, this work represents a novel investigation of CH₄ line mixing at elevated temperatures and, perhaps more importantly, the temperature-scalable empirical models which were developed in this work will enable quantitative interpretation of absorption spectroscopy measurements in high-temperature environments.

Declaration of Competing Interest

The authors declare no conflicts of interest.

CRediT authorship contribution statement

Jidong Li: Conceptualization, Data curation, Formal analysis, Investigation, Methodology, Software, Validation, Visualization, Writing - original draft, Writing - review & editing. Anil P. Nair: Conceptualization, Formal analysis, Investigation, Software, Writing - original draft, Writing - review & editing. Kevin K. Schwarm: Investigation, Resources, Writing - original draft, Writing - review & editing. Daniel I. Pineda: Conceptualization, Investigation, Project administration, Resources, Supervision, Visualization, Writing - original draft, Writing - review & editing. R. Mitchell Spearrin: Conceptualization, Funding acquisition, Project administration, Resources, Supervision, Validation, Writing - original draft, Writing - review & editing.

Acknowledgements

This work was supported by the U.S. National Science Foundation, CAREER Award No. 1752516. Supplementary support was provided by the Air Force Office of Scientific Research (AFOSR) Young Investigator Program (YIP) award no. FA9550-19-1-0062 with Dr. Chiping Li as Program Officer. JL gratefully acknowledges The Statesponsored Postgraduate Program for Building High-level Universities by China Scholarship Council (No. 201906210368) as well as

continuous support from Dr. Zhiming Peng (Tsinghua University). KKS acknowledges support from the Department of Defense (DoD) through the National Defense Science & Engineering Graduate Fellowship (NDSEG) Program. DIP is supported in part by NSF AGEP Award No. 1306683.

Appendix A. Uncertainty analysis

The uncertainty analysis presented here follows the analysis presented in the Appendix of Bendana et al [44]. The MEG law coefficients reported in Table 1 and the first-order line mixing coefficients reported in Table 2 are provided with uncertainty estimates, the calculations of which are detailed in this Appendix.

A1. Thermodynamic state variables

The parameters we report are determined from measurements made at various thermodynamic conditions, uncertainties of which ultimately affect the temperature- and pressure-dependence of the associated models.

Uncertainty in pressure, ΔP is generally dominated by two sources. For both shock tube and heated optical cell experiments, uncertainty in the pressure transducer/capacitance manometer measurements ΔP_{meas} leads to uncertainties in line mixing parameters. For the shock tube experiments, uncertainty in the reflected shock pressure P5 due to uncertainties associated with the shock relations ΔP_5 contribute.

$$\left(\frac{\Delta P}{P}\right)^2 = \left(\frac{\Delta P_{meas}}{P_{meas}}\right)^2 + \left(\frac{\Delta P_5}{P_5}\right)^2 \tag{A.1}$$

For the heated optical static gas cell experiments, ΔP_5 is taken to be zero, and ΔP_{meas} is 0.12% of the measurement reported by the capacitance manometer, while for the shock tube experiments, ΔP_{meas} is 0.18% of the measurement reported by the pressure transducer

Uncertainty in temperature, ΔT , is different for each of the devices. For the shock tube measurements, the uncertainty in temperature is the uncertainty in reflected shock temperature T_5 , ΔT_5 . For brevity, the ΔP_5 and ΔT_5 are not discussed here in further detail; however, we note that significant contributors include uncertainties in the composition of the driven gas (from the barometric mixture preparation), uncertainties in the time-of-arrival measurements, and small uncertainties in the initial pressure P_1 and temperature T_1 . Further information regarding the calculation of uncertainties in reflected shock conditions can be found in the work by Campbell et al[62].

Temperature uncertainty in the static optical cell measurements is $\Delta T_{meas} = 10$ K, based on the uncertainty of thermocouple measurements taken on the outside surface of the cell. More detail about the optical cell used in this paper is available in previous work [53].

A2. The first-order line mixing coefficients

A nonlinear regression fitting routine (The nlinfit function in MATLAB) was used to fit the experimental absorbance to obtain the first-order line mixing coefficients. The uncertainties in Tables 1 and 2 were determined as the single-sigma confidence interval calculated using the estimated Jacobian matrix of the nonlinear regression and the estimated variance-covariance matrix for the fitted parameters. It should be noted that the uncertainties of the broadening coefficients and temperature exponents in the HITEMP database may also increase the uncertainties of line mixing coefficients since these were assumed as fixed in our spectral fitting routines. The uncertainties for the broadening coefficients of

the studied transitions in R(15) manifold are all given as $\geq 20\%$ and those of the temperature-dependent exponents are given as 2%-20%. Although it is not included in our uncertainty calculation, it is an important source of uncertainty for the line mixing coefficients.

The uncertainties in line mixing coefficients $Y(T_0)$, $\Delta Y(T_0)$, and the temperature dependent exponent n, Δn are determined from applying a linear regression to Eq. (20). In this case, the standard errors of the slopes and intercepts of the fitted lines are Δn and $\Delta Y(T_0)$, respectively. In our linear regressions, we follow the approach of York. et. al [58], incorporating variable uncertainties in both x and y to provide slope and intercept standard errors more reflective of variable measurement quality among the data. In practice, this allows for us to utilize measurements from both the heated static optical cell and the shock tube in the same regression, despite that each of these devices has different measurement uncertainties in thermodynamic state variables.

A3. MEG Law line mixing coefficients

The MEG coefficients $a_1(T)$, a_2 , and a_3 for each experiment are also empirically determined by a nonlinear least-squares fit and the uncertainties of these coefficients were estimated by comparing the parameters retrieved with and without accounting for the line mixing of the weak transitions in the fitting procedure. The differences between the values of a_i determined when the weak transitions were calculated using Lorenzian profile and the values of a_i determined when these were included in the MEG law in each manifold were taken to conservatively estimate Δa_i . This represents the uncertainties associated with the contribution of the weak lines on the line mixing behaviour of the entire manifold. The uncertainties for $a_1(T)$, $\Delta a_1(T)$, together with ΔT are used in the linear regression determination of $a_1(T_0)$ and m to obtain their respective uncertainties $\Delta a_1(T_0)$ and Δm using the same approach of York et al. [58].

References

- Neill T, Judd D, Veith E, Rousar D. Practical uses of liquid methane in rocket engine applications. Acta Astronaut 2009;65(5–6):696–705. doi:10.1016/ i.actaastro.2009.01.052.
- [2] Bendana FA, Lee DD, Schumaker SA, Danczyk SA, Spearrin RM. Cross-band infrared laser absorption of carbon monoxide for thermometry and species sensing in high-pressure rocket flows. Appl Phys B 2019;125(11):204. doi:10.1007/ s00340-019-7320-y.
- [3] Sur R, Wang S, Sun K, Davidson DF, Jeffries JB, Hanson RK. High-sensitivity interference-free diagnostic for measurement of methane in shock tubes. J Quant Spectrosc Radiat Transfer 2015;156:80-7. doi:10.1016/j.jqsrt.2015.01.023.
- [4] Karion A, Sweeney C, Pétron G, Frost G, Michael Hardesty R, Kofler J, et al. Methane emissions estimate from airborne measurements over a western United States natural gas field. Geophys Res Lett 2013;40(16):4393–7. doi:10. 1002/grl.50811.
- [5] Schneising O, Burrows JP, Dickerson RR, Buchwitz M, Reuter M, Bovensmann H. Remote sensing of fugitive methane emissions from oil and gas production in north american tight geologic formations. Earth's Future 2014;2(10):548–58. doi:10.1002/2014ef000265.
- [6] Jacob DJ, Turner AJ, Maasakkers JD, Sheng J, Sun K, Liu X, et al. Satel-lite observations of atmospheric methane and their value for quantifying methane emissions. Atmos Chem Phys 2016;16(22):14371–96. doi:10.5194/acp-16-14371-2016.
- [7] Tomasko MG, Bézard B, Doose L, Engel S, Karkoschka E. Measurements of methane absorption by the descent imager/spectral radiometer (DISR) during its descent through Titan's atmosphere. Planet Space Sci 2008;56(5):624–47. doi:10.1016/j.pss.2007.10.009.
- [8] Karkoschka E, Tomasko MG. Methane absorption coefficients for the Jovian planets from laboratory, Huygens, and HST data. Icarus 2010;205(2):674–94. doi:10.1016/j.icarus.2009.07.044.
- [9] Nassar R, Bernath P. Hot methane spectra for astrophysical applications. Journal of Quantitative Spectroscopy and Radiative Transfer 2003;82(1-4):279–92. doi:10.1016/S0022-4073(03)00158-4. https://linkinghub.elsevier.com/retrieve/pii/S0022407303001584
- [10] Swain MR, Vasisht G, Tinetti G. The presence of methane in the atmosphere of an extrasolar planet. Nature 2008;452(7185):329–31. doi:10.1038/nature06823.
- [11] Fletcher SEM, Schaefer H. Rising methane: a new climate challenge. Science 2019;364(6444):932–3. doi:10.1126/science.aax1828.

- [12] Plant G, Kort EA, Floerchinger C, Gvakharia A, Vimont I, Sweeney C. Large fugitive methane emissions from urban centers along the U.S. east coast. Geophys Res Lett 2019;46(14):8500–7. doi:10.1029/2019GL082635.
- [13] Nagali V, Chou SI, Baer DS, Hanson RK, Segall J. Tunable diode-laser absorption measurements of methane at elevated temperatures. Appl Opt 1996;35(21):4026. doi:10.1364/ao.35.004026.
- [14] Ebert V, Fernholz T, Giesemann C, Pitz H, Teichert H, Wolfrum J, et al. Simultaneous diode-laser-based in situ detection of multiple species and temperature in a gas-fired power plant. Proc Combust Inst 2000;28(1):423–30. doi:10.1016/s0082-0784(00)80239-8.
- [15] Sur R, Sun K, Jeffries JB, Hanson RK. Multi-species laser absorption sensors for in situ monitoring of syngas composition. Appl Phys B 2014;115(1):9–24. doi:10.1007/s00340-013-5567-2.
- [16] Pyun SH, Cho J, Davidson DF, Hanson RK. Interference-free mid-IR laser absorption detection of methane. Meas Sci Technol 2011;22(2). doi:10.1088/0957-0233/22/2/025303.
- [17] Sajid MB, Javed T, Farooq A. High-temperature measurements of methane and acetylene using quantum cascade laser absorption near $8\mu m$. J Quant Spectrosc Radiat Transfer 2015;155:66–74. doi:10.1016/j.jqsrt.2015.01.009.
- [18] Sajid MB, Javed T, Farooq A. Shock tube/laser absorption measurements of methane, acetylene and ethylene during the pyrolysis of n-pentane and isopentane. Combust Flame 2016;164:1–9. doi:10.1016/j.combustflame.2015.10.
- [19] Zhang G, Khabibullin K, Farooq A. An IH-QCL based gas sensor for simultaneous detection of methane and acetylene. Proc Combust Inst 2019;37(2):1445–52. doi:10.1016/j.proci.2018.06.062.
- [20] Wei C, Schwarm KK, Pineda DI, Spearrin RM. Deep neural network inversion for 3D laser absorption imaging of methane in reacting flows. Opt Lett 2020;45(8):2447–50. doi:10.1364/ol.391834.
- [21] Ghysels M, Vasilchenko S, Mondelain D, Béguier S, Kassi S, Campargue A. Laser absorption spectroscopy of methane at 1000 K near 1.7 μ m: a validation test of the spectroscopic databases. J Quant Spectrosc Radiat Transfer 2018;215:59–70. doi:10.1016/j.jqsrt.2018.04.032.
- [22] Borysov A, Champion JP, Jørgensen UG, Wenger C. Towards simulation of high temperature methane spectra. Mol Phys 2002;100(22):3585–94. doi:10.1080/ 00268970210161430.
- [23] Hargreaves RJ, Gordon IE, Rey M, Nikitin AV, Tyuterev VG, Kochanov RV, et al. An accurate, extensive, and practical line list of methane for the HITEMP database. Astrophys J Suppl Ser 2020;247(2):55. doi:10.3847/1538-4365/ ab7a1a.
- [24] Hartmann JM, Boulet C, Robert D. Collisional effects on molecular spectra. Elsevier; 2008. doi:10.1016/B978-0-444-52017-3.X0001-5.
- [25] Benner DC, Rinsland CP, Devi VM, Smith MAH, Atkins D. A multispectrum least fitting technique. J Quant Spectrosc Radiat Transfer 1995;53(6):705–21.
- [26] Pine A. Line mixing sum rules for the analysis of multiplet spectra. Journal of Quantitative Spectroscopy and Radiative Transfer 1997;57(2):145–55. doi:10.1016/S0022-4073(96)00129-X. https://linkinghub.elsevier.com/retrieve/pii/S002240739600129X
- [27] Pine A. N₂ and Ar broadening and line mixing in the P and Rbranches of the v₃ band of CH₄. J Quant Spectrosc Radiat Transfer 1997;57(2):157–76. doi:10.1016/S0022-4073(96)00130-6. https://linkinghub.elsevier.com/retrieve/ pii/S0022407396001306
- [28] Pieroni D, Nguyen-Van-Thanh, Brodbeck C, Claveau C, Valentin A, Hartmann JM, et al. Experimental and theoretical study of line mixing in methane spectra. i. the N_2 -broadened ν_3 band at room temperature. J Chem Phys 1999;110(16):7717–32. doi:10.1063/1.478724.
- [29] Pieroni D, Nguyen-Van-Thanh, Brodbeck C, Hartmann J-M, Gabard T, Champion J-P, et al. Experimental and theoretical study of line mixing in methane spectra. II. influence of the collision partner (He and Ar) in the v₃ IR band. J Chem Phys 1999;111(15):6850–63. doi:10.1063/1.480095.
- [30] Pine AS, Gabard T. Speed-dependent broadening and line mixing in CH₄ perturbed by Ar and N₂ from multispectrum fits. J Quant Spectrosc Radiat Transfer 2000;66(1):69–92. doi:10.1016/S0022-4073(99)00222-8.
- [31] Grigoriev IM, Filippov NN, Tonkov MV, Gabard T, Le Doucen R. Estimation of line parameters under line mixing effects: the v₃ band of CH₄ in helium. J Quant Spectrosc Radiat Transfer 2001;69(2):189–204. doi:10.1016/S0022_4003(00)00076_5
- [32] Grigoriev IM, Filippov NN, Tonkov MV, Champion JP, Gabard T, Le Doucen R. Line parameters and shapes of high clusters: R branch of the ν_3 band of CH₄ in He mixtures. J Quant Spectrosc Radiat Transfer 2002;74(4):431–43. doi:10. 1016/S0022-4073(01)00263-1.
- [33] Pine AS, Gabard T. Multispectrum fits for line mixing in the v₃ band Q branch of methane. J Mol Spectrosc 2003;217(1):105–14. doi:10.1016/S0022-2852(02) 00011-5.
- [34] Tran H, Flaud PM, Gabard T, Hase F, von Clarmann T, Camy-Peyret C, et al. Model, software and database for line-mixing effects in the ν_3 and ν_4 bands of CH₄ and tests using laboratory and planetary measurements-I: N₂ (and air) broadenings and the earth atmosphere. J Quant Spectrosc Radiat Transfer 2006;101(2):284–305. doi:10.1016/j.jqsrt.2005.11.020.
- [35] Tran H, Flaud PM, Fouchet T, Gabard T, Hartmann JM. Model, software and database for line-mixing effects in the ν_3 and ν_4 bands of CH₄ and tests using laboratory and planetary measurements-II: H₂ (and He) broadening and the atmospheres of Jupiter and Saturn. J Quant Spectrosc Radiat Transfer 2006;101(2):306–24. doi:10.1016/j.jqsrt.2005.11.033.
- [36] Mondelain D, Payan S, Deng W, Camy-Peyret C, Hurtmans D, Mantz AW. Measurement of the temperature dependence of line mixing and pressure broad-

- ening parameters between 296 and 90 K in the v_3 band of 12 CH₄ and their influence on atmospheric methane retrievals. J Mol Spectrosc 2007;244(2):130–7. doi:10.1016/j.ims.2007.05.005.
- [37] Ghysels M, Gomez L, Cousin J, Tran H, Amarouche N, Engel A, et al. Temperature dependences of air-broadening, air-narrowing and line-mixing coefficients of the methane v₃ R(6) manifold lines—Application to in-situ measurements of atmospheric methane. J Quant Spectrosc Radiat Transfer 2014;133:206–16. doi:10.1016/j.jqsrt.2013.08.003.
- [38] Mendonca J, Strong K, Sung K, Devi VM, Toon GC, Wunch D, et al. Using high-resolution laboratory and ground-based solar spectra to assess CH₄ absorption coefficient calculations. J Quant Spectrosc Radiat Transfer 2017;190:48–59. doi:10.1016/j.jqsrt.2016.12.013.
- [39] Devi VM, Benner DC, Gamache RR, Tran H, Smith MAH, Sams RL. Multispectrum analysis of air-broadened spectra in the ν₃ Q branch of ¹²CH₄. J Quant Spectrosc Radiat Transfer 2018;206:409–29. doi:10.1016/j.jqsrt.2017.12.005.
- [40] Pine A. Speed-dependent line mixing in the ν3 band Qbranch of methane. Journal of Quantitative Spectroscopy and Radiative Transfer 2019;224:62–77. doi:10.1016/j.jqsrt.2018.10.038. https://linkinghub.elsevier.com/retrieve/pii/S0022407318306253
- [41] Rosenkranz P. Shape of the 5mm oxygen band in the atmosphere. IEEE Transactions on Antennas and Propagation 1975;23(4):498–506. doi:10.1109/TAP. 1975.1141119. http://ieeexplore.ieee.org/document/1141119/
- [42] Millot G, Lavorel B, Steinfeld JI. Collisional broadening, line shifting, and line mixing in the stimulated raman $2\nu_2$ Q branch of CH₄. J Chem Phys 1991;95(11):7938–46. doi:10.1063/1.461322.
- [43] Rosasco GJ, Rahn LA, Hurst WS, Palmer RE, Dohne SM. Measurement and prediction of raman q branch line selfbroadening coefficients for CO from 400 to 1500 K. J Chem Phys 1989;90(8):4059–68. doi:10.1063/1.455764.
- [44] Bendana FA, Lee DD, Wei C, Pineda DI, Spearrin RM. Line mixing and broadening in the v(1→3) first overtone bandhead of carbon monoxide at high temperatures and high pressures. J Quant Spectrosc Radiat Transfer 2019;239:106636. doi:10.1016/j.jqsrt.2019.106636.
- [45] Lee DD, Bendana FA, Nair AP, Pineda DI, Spearrin RM. Line mixing and broadening of carbon dioxide by argon in the v₃ bandhead near 4.2 μm at high temperatures and high pressures. Journal of Quantitative Spectroscopy and Radiative Transfer 2020:107135. doi:10.1016/j.jqsrt.2020.107135. https://linkinghub.elsevier.com/retrieve/pii/S0022407320301151
- [46] Polanyi JC, Woodall KB. Mechanism of rotational relaxation. J Chem Phys 1972;56(4):1563–72. doi:10.1063/1.1677406.
- [47] Koszykowski ML, Rahn LA, Palmer RE, Coltrin ME. Theoretical and experimental studies of high-resolution inverse raman spectra of N₂ at 1–10 atm. J Phys Chem 1987;91(1):41–6. doi:10.1021/j100285a012.
- [48] Li J, Du Y, Peng Z, Ding Y. Measurements of spectroscopic parameters of CO₂ transitions for Voigt, Rautian, Galatry and speed-dependent Voigt profiles near 1.43 μm using the WM-DAS method. J Quant Spectrosc Radiat Transfer 2019;224:197–205. doi:10.1016/j.jqsrt.2018.11.014.
- [49] Li J, Peng Z, Ding Y. Wavelength modulation-direct absorption spectroscopy combined with improved experimental strategy for measuring spectroscopic parameters of H₂O transitions near 1.39 μm. Opt Lasers Eng 2020;126(August 2019):105875. doi:10.1016/j.optlaseng.2019.105875.
- [50] Smith EW. Absorption and dispersion in the O₂ microwave spectrum at atmospheric pressures. J Chem Phys 1981;74(12):6658-73. doi:10.1063/1.441112.
- [51] Ben-Reuven A. Impact broadening of microwave spectra. Phys Rev 1966;145(1):7–22. doi:10.1103/PhysRev.145.7.
- [52] Steinfeld JI, Ruttenberg P, Millot G, Fanjoux G, Lavorel B. Scaling laws for inelastic collision processes in diatomic molecules. J Phys Chem 1991;95(24):9638–47. doi:10.1021/j100177a010.
- [53] Schwarm KK, Dinh HQ, Goldenstein CS, Pineda DI, Spearrin RM. High-pressure and high-temperature gas cell for absorption spectroscopy studies at wavelengths up to 8 μ m. J Quant Spectrosc Radiat Transfer 2019;227:145–51. doi:10.1016/j.jqsrt.2019.01.029.
- [54] Brown LR, Sung K, Benner DC, Devi VM, Boudon V, Gabard T, et al. Methane line parameters in the HITRAN2012 database. J Quant Spectrosc Radiat Transfer 2013;130:201–19. doi:10.1016/j.jqsrt.2013.06.020.
- [55] Pineda DI, Bendana FA, Schwarm KK, Spearrin RM. Multi-isotopologue laser absorption spectroscopy of carbon monoxide for high-temperature chemical kinetic studies of fuel mixtures. Combust Flame 2019;207:379–90. doi:10.1016/ j.combustflame.2019.05.030.
- [56] Anderson JD. Modern compressible flow. 3rd. McGraw-Hill; 2002.
- [57] Campbell MF, Wang S, Goldenstein CS, Spearrin RM, Tulgestke AM, Zaczek LT, et al. Constrained reaction volume shock tube study of n -heptane oxidation: Ignition delay times and time-histories of multiple species and temperature. Proceedings of the Combustion Institute 2015;35(1):231–9. doi:10.1016/j.proci. 2014.05.001. http://linkinghub.elsevier.com/retrieve/pii/S1540748914000042
- [58] York D, Evensen NM, Martinez ML, De Basabe Delgado J. Unified equations for the slope, intercept, and standard errors of the best straight line. Am J Phys 2004;72(3):367–75. doi:10.1119/1.1632486.
- [59] Lisak D, Hodges JT, Ciuryło R. Comparison of semiclassical line-shape models to rovibrational H₂O spectra measured by frequency-stabilized cavity ring-down spectroscopy. Phys Rev A - Atomic Mol Opt Phys 2006;73(1):1–13. doi:10.1103/ PhysRevA.73.012507.
- [60] Li J, Du Y, Ding Y, Peng Z. Experimental and simulated study of line-shape models for measuring spectroscopic parameters using the WM-DAS method part I: Collisional broadening and absorption coefficients of H₂O-Ar system. J Quant Spectrosc Radiat Transfer 2020;254:107216. doi:10.1016/j.jqsrt.2020. 107216.

- [61] Goldenstein CS, Hanson RK. Diode-laser measurements of linestrength and temperature-dependent lineshape parameters for $\rm H_2O$ transitions near 1.4 μm using Voigt, Rautian, Galatry, and speed-dependent Voigt profiles. J Quant Spectrosc Radiat Transfer 2015;152:127–39. doi:10.1016/j.jqsrt.2014.11.008.
- [62] Campbell MF, Owen KG, Davidson DF, Hanson RK. Dependence of calculated postshock thermodynamic variables on vibrational equilibrium and input uncertainty. J Thermophys Heat Transfer 2017;31(3):586–608. doi:10.2514/1.74952.